PASJ: Publ. Astron. Soc. Japan **63**, S415–S435, 2011 March 25

Discovery of an Excess of Hα Emitters around 4C 23.56 at $z = 2.48$

Ichi TANAKA,[1] Carlos DE BREUCK,[2] Jaron D. KURK,[3] Yoshiaki TANIGUCHI,[4] Tadayuki KODAMA,[1,5] Yuichi MATSUDA,[6] Chris PACKHAM,[7] Andrew ZIRM,[8] Masaru KAJISAWA,[5,9] Takashi ICHIKAWA,[9] Nick SEYMOUR,[10] Daniel STERN,[11] Alan STOCKTON,[12] Bram P. VENEMANS,[2] and Joël VERNET[2]

[1]*Subaru Telescope, National Astronomical Observatory of Japan, 650 North A'ohoku Place, Hilo, HI 96720, USA*
ichi@subaru.naoj.org

[2]*European Southern Observatory, Karl-Schwarzschild Strasse 2, 85748 Garching bei München, Germany*

[3]*Max-Planck-Institut für extraterrestrische Physik, Postfach 1312, 85741 Garching, Germany*

[4]*Research Center for Space and Cosmic Evolution, Ehime University, Bunkyo-cho 2-5, Matsuyama 790-8577*

[5]*National Astronomical Observatory of Japan, 2-21-1 Osawa, Mitaka, Tokyo 181-8588*

[6]*Department of Physics, University of Durham, South Road, Durham DH1 3LE, UK*

[7]*Department of Astronomy, University of Florida, 211 Bryant Science Center, P.O. Box 112055, Gainesville, FL 32611-2055, USA*

[8]*Dark Cosmology Centre, Niels Bohr Institute, University of Copenhagen, Juliane Maries Vej 30, DK-2100 Copenhagen, Denmark*

[9]*Astronomical Institute, Graduate School of Science, Tohoku University, Aramaki, Aoba, Sendai 980-8578*

[10]*Mullard Space Science Laboratory, UCL, Holmbury St Mary, Dorking, Surrey, RH5 6NT, UK*

[11]*Jet Propulsion Laboratory, California Institute of Technology, 4800 Oak Grove Dr., Pasadena, CA 91109, USA*

[12]*Institute for Astronomy, University of Hawaii, Honolulu, HI 96822, USA*

(Received 2010 September 13; accepted 2010 December 7)

Abstract

We report on the discovery of a significant excess of candidate Hα emitters (HAEs) in the field of the radio galaxy 4C 23.56 at $z = 2.483$. Using the MOIRCS near-infrared imager on the Subaru Telescope we found 11 candidate emission-line galaxies to a flux limit of $\sim 7.5 \times 10^{-17}$ erg s^{-1} cm^{-2}, which is about 5-times excess from the expected field counts with an ~ 3-σ significance. Three of these have been spectroscopically confirmed as redshifted Hα at $z = 2.49$. The distribution of candidate emitters on the sky is tightly confined to a 1.2-Mpc-radius area at $z = 2.49$, locating 4C 23.56 at the western edge of the distribution. An analysis of the deep Spitzer MIPS 24 μm imaging shows that there is also an excess of faint MIPS sources. All but two of the 11 HAEs are also found in the MIPS data. The inferred star-formation rate (*SFR*) of the HAEs based on the extinction-corrected Hα luminosity (median $SFR \gtrsim 100\,M_\odot\,\mathrm{yr}^{-1}$) is similar to those of HAEs in random fields at $z \sim 2$. On the other hand, the MIPS-based *SFR* for the HAEs is on average 3.6-times larger, suggesting the existence of star-formation significanly obscured by dust. A comparison of the Hα-based star-formation activities of the HAEs in the 4C 23.56 field to those in another proto-cluster around PKS 1138−262 at $z = 2.16$ reveals that the latter tend to have fainter Hα emission despite similar K-band magnitudes. This suggests that star-formation may be suppressed in the PKS 1138−262 protocluster relative to the 4C 23.56 protocluster. This difference among the HAEs in the two proto-clusters at $z > 2$ may imply that some massive cluster galaxies are just forming at these epochs with some variation among them.

Key words: galaxies: Hα emitters — galaxies: high redshifts — galaxies: individual (4C 23.56) — galaxies: protocluster

1. Introduction

Clusters of galaxies are the most massive bound systems in the universe. The present-day cluster population is dominated by early-type galaxies, which make up a tight "red sequence" in the color–magnitude diagram (Dressler 1980). Analyses of the zero-point, slope, and scatter of the color–magnitude relation have been playing key roles in understanding when and how galaxies in clusters are formed and evolved (e.g., Bower et al. 1992).

Studies of low-to-intermediate redshift clusters indicate that the majority of stars in cluster galaxies are formed at $z > 2$ (e.g., Ellis et al. 1997; Bower et al. 1998; Kodama et al. 1998; Stanford et al. 1998; Holden et al. 2004; Tran et al. 2007). On the other hand, detailed morphological analyses of cluster red galaxies suggest that a significant fraction of the present-day cluster early-type galaxies must have been fully assembled after $z \sim 1$ (e.g., Dressler et al. 1997; van Dokkum et al. 2000; van Dokkum & Franx 2001; Ellis et al. 2006; Mei et al. 2009). A significant rise in star-formation activity in the cluster cores is also seen as one goes to higher ($z > 0.4$) redshift, the "Butcher–Oemler effect" (Butcher & Oemler 1978, 1984).

Studies of the Butcher–Oemler effect, as well as the morphological transformation in cluster cores, have been among the major topics in extragalactic astronomy for the past two decades (e.g., Dressler et al. 1994; Couch et al. 1994; Dressler et al. 1997; Balogh et al. 1997; Oemler et al. 1997; Poggianti et al. 1999; van Dokkum et al. 2000; Ellingson et al. 2001; Kodama & Bower 2001; Mei et al. 2009; Pannella et al. 2009). As the observational data have been accumulated for ever more distant galaxy clusters, the "break" of the red sequence at

fainter magnitudes and its evolution has attracted great attention (e.g., Kajisawa et al. 2000; Kodama et al. 2004; De Lucia et al. 2004; Tanaka et al. 2005; De Lucia et al. 2007; Gilbank et al. 2008). These phenomena have been discussed within the framework of the "down-sizing" of the star-formation activity, whereby the stellar mass of the galaxies that host star formation at a fixed rate is, on average, decreasing with cosmic time. The evolution of the faint end of the red sequence is also connected to a continuous infall of star-forming galaxies into the cluster cores, their subsequent cessation of star-formation, and change in their morphologies (Poggianti et al. 2004; Bundy et al. 2006).

From the local universe to intermediate redshifts ($z < 1$), a number of studies suggest that star formation is strongly suppressed in the cluster cores compared with the low-density field environment (e.g., Hashimoto et al. 1998; Gómez et al. 2003; Nakata et al. 2005; Poggianti et al. 2006; Patel et al. 2009). For passively-evolving early-type galaxies, there is also weak, but growing, evidence that the luminosity-weighted ages of galaxies tend to be older in higher density environments. This suggests that perhaps the time scale of star formation and/or secondary episodes of the star formation vary with environment (Thomas et al. 2005; Clemens et al. 2006; Rakos et al. 2008; Clemens et al. 2009; Blanton & Moustakas 2009; Pannella et al. 2009; Thomas et al. 2010). Recently, however, this trend is observed to flatten or even reverse, with the density dependence of star-formation disappearing or with enhanced star-formation in the cluster core at $z > 1$ (Elbaz et al. 2007; Ideue et al. 2009; Hayashi et al. 2010; Tran et al. 2010).

If the majority of the massive cluster galaxies ($M_\star > 10^{10}\,M_\odot$) begin forming their stars at $z > 2$, they will have high star formation rates at higher redshifts. Hayashi et al. (2010) have surveyed star-forming galaxies in the X-ray cluster XMMXCS J2215.9−1738 at $z = 1.46$ using a narrowband filter that samples the redshifted [O II] doublet located at the cluster redshift. They showed that the [O II] emitting star-forming galaxies are prevalent everywhere in the cluster, including its core region (see also, Hilton et al. 2010). Although star formation is still confined to the cluster outskirts in other $z \sim 1.4$ clusters (Lidman et al. 2008; Bauer et al. 2011; Strazzullo et al. 2010), the widespread star formation in XMMXCS J2215.9−1738 is in strong contrast to similar surveys of lower redshift clusters at $z = 0.81$ and $z = 0.41$ (Kodama et al. 2004; Koyama et al. 2010). The color–magnitude relation for XMMXCS J2215.9−1738 also shows a larger scatter than those of other intermediate redshift clusters (Hilton et al. 2009; Papovich et al. 2010). Although we need a larger sample of clusters at intermediate and high redshifts to discern a general trend in the star formation–galaxy density relation (Elbaz et al. 2007; Poggianti et al. 2008; Sobral et al. 2011), the existence of widespread star-formation activity in this $z = 1.5$ cluster strongly suggests that we are gradually approaching a major epoch of galaxy formation in cluster environments.

At higher redshifts ($z > 2$), the number of the known (proto-) clusters is still quite small, and the majority of known proto-clusters were discovered in narrowband Lyα-emitter surveys. With some exceptions (e.g., Steidel et al. 1998, 2000; Shimasaku et al. 2003; Steidel et al. 2005; Gobat et al. 2011), much of the search for proto-clusters has been done around powerful radio galaxies and QSOs with known redshifts (e.g., Keel et al. 1999; Pentericci et al. 2000; Kurk et al. 2000; Yamada et al. 2001; Venemans et al. 2002; Kurk et al. 2004a; Venemans et al. 2005, 2007; Matsuda et al. 2009). The success of these searches around radio galaxies is related to the fact that the host galaxies of powerful radio sources tend to be the most massive galaxies at any epoch of the universe (De Breuck et al. 2002; Seymour et al. 2007). Powerful radio sources are powered by central super-massive black holes, and the large inferred masses of the black holes in turn imply massive host stellar systems (Magorrian et al. 1998). The largest galaxies in the universe tend to lie in the centers of largest-scale haloes which must have originated from the primordial density peaks where galaxy formation processes are accelerated in a biased way (Rees 1985).

Recently, Tanaka et al. (2010) analyzed the broadband SED of galaxies in the PKS 1138 proto-cluster, and found that proto-cluster galaxies show suppressed star-formation on average compared to field galaxies (see also, Zirm et al. 2008; Doherty et al. 2010). This implies that even at $z \gtrsim 2$ the activity in the cluster core region seems to lag behind the star-formation activity we see in galaxies in field surveys. Steidel et al. (2000) also reported older stellar ages for their $z = 2.3$ proto-cluster than for field galaxies in the same survey, implying a similar trend. The detection of a possible (proto-) red-sequence in four known proto-cluster fields at $z \gtrsim 2$ via *JHK* photometry (Kodama et al. 2007) also indicates that, though the star-formation is also likely to be prevalent there, some K-bright galaxies may already be converging to the red-sequence.

At higher redshifts, there are some hints that more intense star-formation is occurring, even in the proto-cluster environment. In the SSA22 field, which is known to contain a large overdensity of galaxies at $z = 3.1$ (Steidel et al. 1998, 2000), Matsuda et al. (2004) detected a significant number of the extended Lyα blobs that are thought to be progenitors of massive galaxies (e.g., Dijkstra & Loeb 2009). Two of the largest Lyα blobs are identified with red, massive ($M_\star \sim 10^{11}\,M_\odot$) galaxies, comparable to dominant cluster galaxies at $z < 1.5$ (Uchimoto et al. 2008; Stott et al. 2010). Tamura et al. (2009) have detected an excess of AzTEC 1.1 mm-sources in the same SSA22 field. The positional correlation of the AzTEC sources with the Lyα emitter distribution at $z = 3.1$ suggests that dust-enshrouded vigorous star-formation might be going on in the field. There is also a report of a significant excess of submm-bright objects in the TNJ 1338−1942 field at $z = 4.1$, which is known to have a proto-cluster identified by Lyα emitters (De Breuck et al. 2004; Venemans et al. 2007).

As was demonstrated by Kodama and Bower (2001), star formation activity in cluster cores should have been as vigorous as in the field environment at some point in the past (and may exceed it at even higher redshifts). To observe this crossover point we need larger samples of proto-clusters at $z = 2$–4.

The field around 4C 23.56 is one of the most promising proto-cluster candidates at $z > 2$ (Knopp & Chambers 1997, hereafter KC97). The authors detected an excess of candidate Lyα emitters as well as an excess of very red objects in

$I - K'$ color in their survey field (1.25 arcmin^2). More recently, Kajisawa et al. (2006a) took deep J and K_s images with CISCO on Subaru and found a significant excess of Distant Red Galaxies (DRGs: Franx et al. 2003) in a 1.′6 × 1.′6 field. This further supports the idea that there are a number of evolved galaxies in this proto-cluster at $z \sim 2.49$. However, both of these surveys have very limited field coverage, and they may not be probing the whole picture of the proto-cluster. So far no other follow-up observations, including any redshift confirmation, have been reported in the literature.

Here we present the result of our new Hα emitter (HAE) search around 4C 23.56 with the wide-field near-infrared imager, MOIRCS, mounted on the 8.2 m Subaru Telescope. In this study, we show that there is a clear and strong excess of the HAEs near the radio galaxy. We present their star-formation properties and discuss the characteristics of this proto-cluster by comparing with other fields at similar redshifts. Archival Spitzer MIPS data are also used to probe dusty star-forming activity in the proto-cluster. This is the first narrow-band Hα emitter survey of a proto-cluster field at $z > 2$ after Kurk et al. (2004a). The field size we cover is nearly 19-times larger than that of KC97, and is more than twice as large as that of Kurk et al. (2004a). We note that the survey redshift of $z \sim 2.5$ is close to the red end of the Hα-observable window ($z < 2.7$) from the ground, due to a significant rise of the thermal background beyond the K-band window.

Throughout this paper, the standard ΛCDM cosmology with $\Omega_m = 0.3, \Omega_\Lambda = 0.7, h = 0.7$ is assumed (1′ = 1.18 comoving Mpc at $z = 2.48$). All of the magnitudes presented in this paper are in the AB system, unless otherwise noted.

2. Observations and Data Reduction

2.1. Observations

The primary data for the current work were collected using the Multi-Object Infrared Camera and Spectrograph (MOIRCS: Ichikawa et al. 2006; Suzuki et al. 2008) mounted on the Cassegrain focus of the Subaru 8.2-m Telescope at Mauna Kea. The observations were executed during the second half-night of 2007 June 1 UT, during one of the author's (IT) Subaru Staff Time. The weather was photometric, but with variable seeing in the range 0.″47–0.″7.

MOIRCS has two independent sets of optics (including both filters and detectors), which divide the full 4′ × 7′ field of view (FOV) into two subfields (channels 1 and 2), each covering 4′ × 3.′5. We set the MOIRCS position angle to −90° so that the long side (= 7′ side) of the FOV aligns to the east–west direction. In this setting, the channel 1 FOV is on the eastern (left) side (see figure 1b).

We used both the standard K_s-band filter and a narrow-band (*NB*) filter called "CO" or "*NB2288*". The *NB* filter has a central wavelength of $\lambda_c = 2.2881\,\mu$m with a bandwidth of 0.023 μm. Note that these are the post-installation measured values (M. Akiyama, private communication). Individual *NB* exposures were 300 s. In total, we obtained 16 exposures, yielding a total integration time of 4800 s. Shallow data were also acquired in the K_s band to enable continuum subtraction of the *NB* data. The K_s band exposures were taken in 55 s and 3-coadds. We obtained 9 frames in total (1485 s). We found that stars on three images were elongated due to poor guiding at high elevation (> 84°). We rejected those frames during the final combine, resulting in a total integration of 990 s. We applied a standard circular-dither pattern with a diameter of

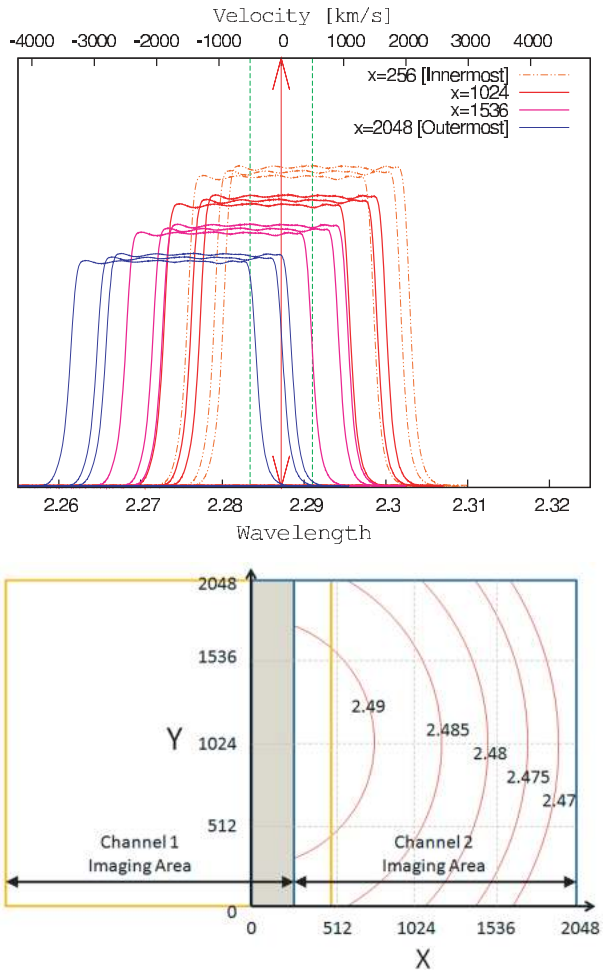

Fig. 1. (Top) Simulated shift of the transmission curve of the *NB2289* filter. The horizontal axis is the wavelengths in μm and the vertical axis has arbitrary units. The curves with orange (dot-dot-dashed), red (thick solid), magenta (thick solid), and blue (thin solid) colors each indicate the transmission curves at $x = 256$ (close to the innermost FOV coverage), 1024 (detector center), 1536, and 2048 (outer edge of the FOV) in channel-2 raw-image coordinates (the bottom figure, and corresponds to the right-half of the MOIRCS FOV). At each x position, the shift of the transmission curve along with y-coordinates is also shown: the curve at the longest wavelength is at the detector center ($y = 1024$), and shifts to shorter wavelengths as the y coordinates goes to the edge of the detector ($y = 512/1536$: middle and 1/2048: bluest). The red arrow indicates the expected position of the Hα emission, and the vertical green lines (dots) indicate the range of the shift for objects at ± 500 km s^{-1} relative to the radio galaxy. The peak amplitude of the transmission curves at each x coordinate are artificially shifted for clarity. See discussion for sub-subsection 2.1.1 for details. (Bottom) Schematic figure of the MOIRCS field of view for explanation of the top figure. The full 4′ × 7′ FOV is divided into two channels. Note that the minimum x coordinate of the raw data area is around $x = 270$ for channel 2 ($x < 270$ is blocked by the mirror shadow). The curves on the channel-2 side show the iso-redshift contours (each number indicates the redshift) we can detect Hα at the central wavelength of the filter window. The *NB2288* filter can cover the redshift range of ±0.017. The pointing center is around (270, 1024).

20″. After the target observation, four position dithered data of the UKIRT FS 151 standard star were acquired in both the K_s and *NB2288* bands.

We note that 4C 23.56 is close ($\sim 1°$) to a bright ($K \sim 0$ mag) Mira-type star. Such bright stars are known to occasionally cause significant stray light on the image.[1] Fortunately, the effect was small during the night. However, stray light was seen in some of the data. It affected only a tiny portion ($< 1\%$) of the total area, and we took care to mark the positions of any stray light before identifying the emitters. Unfortunately, stray light caused a hole-like pattern near the radio galaxy in the K_s data. Due to this, the total magnitude for 4C 23.56 may be systematically wrong. For other targets, we confirmed that stray light does not affect the photometry.

2.1.1. Wavelength shift of NB filters

In general, the central wavelength of *NB* filters will shift with the angle of incidence of the light to the filter surface. In our case, therefore, the observable wavelength window will change with the position of targets on the detector.

In figure 1 we show the simulated shift of the filter transmission curve with source position on the detector (the case for channel 2 is shown here: R. Suzuki 2006, private communication). We find that the redshift range of interest, $2.47 < z < 2.49$, is always covered by $> 80\%$ of the detector area. As a reference, the expected wavelength of the Hα emission from 4C 23.56 is plotted as the arrow in figure 1. Note that the redshift of 4C 23.56 is 2.483 ± 0.003 by Röttgering et al. (1997) from C IV, He II, and C III] lines. The bottom of figure 1 shows the iso-redshift lines of the observable Hα emission for the center of the filter transmission. The iso-redshift line for 2.483 goes across the center of the detector. In the upper panel of figure 1 we show that Hα emission at $\pm 500\,\mathrm{km\,s^{-1}}$ offset from 4C 23.56 can be observed everywhere, but the very edge of the detector. The plot shows that the emitters blueshifted by $\lesssim 1000\,\mathrm{km\,s^{-1}}$ relative to the radio galaxy will leave the filter at the center of the FOV, while for objects redshifted by $\gtrsim 1000\,\mathrm{km\,s^{-1}}$ escape our detection in the outer 1/4 of the detector. Though MOIRCS uses two independent filters for the two channels, the difference in the center wavelength of these two *NB*s is only 3 Å ($\sim 40\,\mathrm{km\,s^{-1}}$ difference at $z = 2.49$). It should not cause any systematics between the channels.

We note that the velocity window of $\pm 500\,\mathrm{km\,s^{-1}}$ is just adequate for cluster member selection. Simulations of X-ray clusters show that the velocity dispersion of rich clusters generally becomes smaller by about a factor of 2 as one goes from $z = 0$ to 3 (e.g., Eke et al. 1998). Also, the previous Hα emitter survey for a dense protocluster at $z = 2.16$ by Kurk et al. (2004b) found a velocity dispersion of only $360\,\mathrm{km\,s^{-1}}$ (narrower than the width of the *NB* filter for their pre-selection), small for the inferred richness of the protocluster. Thus, we would expect to detect a significant fraction of the protocluster Hα emitters within the MOIRCS narrowband window if its dynamical center is at the same redshift and located on 4C 23.56.

2.2. MOIRCS Data Reduction by MCSRED

Data reduction of the MOIRCS science frames was performed using the MCSRED package,[2] the IRAF[3] script pipeline for MOIRCS imaging data developed by one of the authors (IT). Here, we briefly describe the procedures in the pipeline for the potential user's convenience.

The first step is flatfielding the data. We use a self-flat (i.e., making a flatfield image from the dithered object images) for the K_s band. An object mask is essential for making good quality flatfields. To do this, we first make "quasi-flatfielded" images by subtracting the adjacent image in time from the image from which we make the object mask. Such a "quasi-flatfielded" image will show a flat sky and objects in the image as positive–negative pairs. Then, the residual pattern in the sky of each quasi-flatfielded image is further subtracted by fitting a 3rd-order polynomial surface. This procedure is done independently for each quadrant, because MOIRCS is a 4-channel readout system and any pattern related to the sky variation has discontinuities on quadrant boundaries. After replacing all of the negative objects to the sky value, cosmic-ray removal is applied. Each resulting image is then smoothed by a Gaussian kernel after a 3 by 3 boxcar median filter has been applied. At this stage, most objects are clearly seen on the smoothed image except very faint ones. Then, any area that has a signal larger than the threshold of 1.25σ of the original pixel-to-pixel variation is replaced by the "mask" value of 1, with an additional expansion to the area (here we set 5 pixels) for large and bright objects. This quick object mask works well for the usual science exposures. We note that, though we can do the more accurate "second-pass" mask-making procedure after getting the final combined image, the result is almost the same, and is not necessary for our data.

After making the object masks, the flat frame is made from the science data, itself, with the mask applied. For the narrowband data we used dome flat data, as described further below. After flatfielding of the *NB* data, we further subtract the "median sky" image (made with the object masks), which is made from the subset (typically 6 to 10) of the frames before and after the image for the sky subtraction. For the K_s data this procedure can be skipped, because the sky pattern is relatively smooth (by the use of the self flat) and so we can subtract the sky in the next procedure reasonably well. Then, we further subtract any residual sky pattern remaining on each image using a 3rd-order polynomial surface fitting for each quadrant.

The resulting flatfielded, sky-subtracted images are then corrected to remove any geometric distortion. The distortion correction database, which is made from observations of astrometric reference fields, is supplied by the Subaru Observatory. We then measure the position of some (typically 20 to 50) bright and compact objects on each image. The object catalogs for the images are further cross-matched with the catalog for the first image in the input list, and from the result we calculate the offset values which we use to register the images to the first image. Finally, these images are combined, where we weight by the rms^2 of the input image signals.

A note on our *NB2288* reduction: though we usually used the sky- or self-flats for the reduction, we used the dome flat data

[1] See the *Imaging Information* page on MOIRCS website.

[2] MCSRED package is available at ⟨http://www.naoj.org/staff/ichi/MCSRED/mcsred.html⟩.

[3] ⟨http://iraf.noao.edu/⟩.

for correcting the pixel-to-pixel variation of the *NB* data. One reason is because the sky counts in the narrow-band filter are generally low compared with that of broad-band data. There is also the possibility that the sky may not be flat in the *NB* filter. Due to the shift of the observable wavelength window with position (see sub-subsection 2.1.1), the inclusion or exclusion of OH night-sky lines into the window becomes position-dependent. Although there is a small tilt pattern in the dome flats, caused by the difference of the light path between dome data and object data, we estimate that the variation of the photometry due to the use of dome flat is $< 3\%$ (~ 0.033 mag rms) by putting standard stars at several positions across the field of view. This is small compared to our required accuracy.

2.3. Photometry and the Catalog

The object detection and the photometry are done using the "double-image" mode of SExtractor 2.5.0 (Bertin & Arnouts 1996). For the detection image, we used the un-smoothed version of the narrowband data; therefore, our catalog is a simple narrowband-based selection. The K_s image is registered to this, and the seeing size is closely matched (6.0 pixel, $\sim 0\farcs67$ FWHM) for both images. The object detection is done within the area that is covered by more than 12 frames (75%) for *NB2288* as well as 4 frames (67%) for K_s. For the detection parameters, we use the SExtractor DETECT_THRESH = 1.75 and DETECT_MINAREA = 15 with a tophat detection filter (tophat_4.0_5x5.conv).

The effective survey area is 23.6 arcmin^2, which corresponds to a survey volume of 840.7 comoving Mpc^3 at $z = 2.49$, considering our *NB2288* filter bandwidth. We used aperture magnitudes in a diameter of 12 pixels ($= 1\farcs4$ or 11.5 kpc physical scale) for color measurements, and the MAG_AUTO values for derivation of the star-formation rates as well as for the stellar mass (subsection 3.5).

The standard star data for FS 151 were reduced using the same flatfielding data that we used for the object reductions. The instrumental magnitude for FS 151 was measured from the individual 4 frames without combining them, because the images are slightly defocused. These magnitudes were then averaged to obtain the final measurement. The instrumental magnitude for each frame was measured by the "growth-curve" method, which estimates the convergence magnitude with increasing aperture radius. We used the IRAF APPHOT package.

The K_s-band magnitude for FS 151 was taken from Leggett et al. (2006), with the +1.86 conversion from the Vega to AB-magnitude zeropoint applied (Tokunaga & Vacca 2005). For the *NB2288* magnitude, we used the K_s magnitude and the low-dispersion template spectra of a G 3 dwarf star by Wallace and Hinkle (1997). As a final check, we compared the K-band magnitude of some unsaturated stars in our catalog to 2MASS photometry. We found that the magnitudes are well matched at the ~ 0.01 magnitude level with a scatter of ~ 0.1.

Good photometric error estimates are critical for the robust detection of emission-line objects at lower equivalent widths (*EW*s). In our analysis, we used the following two methods. First, we measured the aperture photometry in 1000 random (blank) regions to estimate the $1\,\sigma$ level of the sky variation. This yielded 5-σ limiting magnitudes in a 12-pixel diameter aperture of 22.3 and 22.9 for K_s and *NB2288*, respectively. Second, we estimated the scatter of the $K_s - NB2288$ color introduced by the photometric uncertainty. We generated 70000 fake objects with various magnitudes, and placed them randomly in blank image regions. After rebinning the sample points in 0.5-magnitude intervals of *NB* magnitude, the scatter of the output color excess ($K_s - NB2288$) was evaluated by measuring the distribution's 68% ($1\,\sigma$), 95% ($2\,\sigma$), and 99.7% ($3\,\sigma$) levels directly from the simulation. The result of this simulation was used to estimate of the error on the color excess and for the selection of emitters.

2.4. Supplementary Data Used for Analysis

In the current work, we used some supplementary datasets (subsections 3.1 and 3.4) and here we briefly describe them, though full description will be presented elsewhere (I. Tanaka et al., in preparation).

Deep J-band data were taken using the INGRID camera (Packham et al. 2003) on the William Herschel 4.2-m Telescope (WHT), La Palma. The data were acquired on photometric nights of 2001 September 7 and 8 UT, under good seeing conditions ($\sim 0\farcs6$). The INGRID camera has a HAWAII HgCdTe 1024 × 1024 array, covering roughly $4' \times 4'$ field of view ($= 0\farcs238$/pixel) on the Cassegrain focus of the WHT. The total integration time was 4800 s, resulting in a 50% detection completeness limit of 24.4 mag. The data were reduced in the standard manner, similar to the method for MOIRCS data reduction.

Deep B-band data were taken by the Suprime-cam on Subaru Telescope on the evening of 2009 November 17 UT under clear, but with a marginal seeing condition ($0\farcs9$–$1\farcs2$). It was taken as part of our Ly$\,\alpha$ emitter search in this field. The net exposure time was 4500 s, having a limiting magnitude of 26.5 mag ($5\,\sigma$, $2\farcs5$-diameter aperture). Details of the data reduction as well as the result of the broadband SED fitting analysis are to be described elsewhere (I. Tanaka et al., in preparation).

MOIRCS MOS spectroscopic observations of this field were done on 2006 September 7 UT (S06B-106); i.e., before acquisition of the narrow-band data we describe here. Part of the target selection was done using a similar narrowband survey executed in 2001 September using the INGRID camera on WHT (IT and CP), which should sample the redshift range of $2.429 < z < 2.489$. The conditions were clear, with medium ($\sim 0\farcs8$) seeing conditions. We used the grism with a spectral resolution of ~ 1000 in the K-band window covering the 2.0–2.4 μm spectral range. We used $0\farcs8$ wide slits with typical slit lengths of $\sim 12''$. Each single exposure was 600 s to 1200 s, depending on the airglow line strength. The standard A-B dither pattern was applied during each exposure. In total, 2-hours of integration were gathered. The MOS data reduction was done in the standard manner using the MCSMDP pipeline (pre-release version) by one of the MOIRCS builders. Details of the MOS reduction procedure by MCSMDP can be found in recent paper of Yoshikawa et al. (2010).

Finally, deep 24 μm imaging data from Spitzer/MIPS were obtained as part of the GO program 30240 (PI: A. Stockton). The total exposure time in the central $2' \times 2'$ of the mosaic was approximately 5 ks. The 171 separate exposures each had

a background fitted, and then subtracted before a median of the array was determined. This median was then subtracted from each exposure. The exposures were then mosaicked with MOPEX software[4] with standard inputs and resampling the pixels by a factor of 2.

For the current analysis we focus on a subset of the 24 μm-selected sources that have clear IRAC counterparts. The MIPS photometry was extracted using DAOPHOT in IRAF to fit an empirical PSF model to multiple proximate (within 12″) sources simultaneously. The MIPS source positions were pre-defined using the position of the closest IRAC counterpart. This photometry method mitigated the effects of source confusion.

3. Results

3.1. Emission-Line Object Selection

The selection of Hα emitters at $z \sim 2.5$ is based on excess emission in *NB2288* measured via $K_s - NB2288$ color. In figure 2, we show a color–magnitude diagram for all objects detected in our observations. The overall distribution of the detected objects tends to become broader with increasing magnitudes due to the increasing photometric uncertainty. The intrinsic scatter is also seen for the brighter objects. The intrinsic scatter is caused by the variation in the spectral energy distributions (SEDs) in the K_s band.

The two curves labeled as $\Sigma = 2$ and 3 in figure 2 are the conventionally used measures of the significance of narrowband excess (e.g., Geach et al. 2008). It is formulated as

$$m_K - m_{NB} = -2.5\log[1 - \Sigma\delta 10^{-0.4(m_z - m_{NB})}], \quad (1)$$

where m_z is the zeropoint of the narrowband image and δ is the photometric uncertainty. The $\Sigma = 2$ line generally matches well with our simulated $\sigma = 2$ curve. As the color scatter becomes large at *NB2288* > 22 mag, we limit the selection of emission-line objects to $\Sigma > 2$ and *NB2288* ≤ 22 (corresponding to 7σ level in 12-pixel aperture). We note that the use of our simulated $\sigma = 2$ scattering curve does not change the sample. At *NB2288* > 22, there are actually only a few emission-line object candidates with $\Sigma > 2$, due to the steep rise of the selection curve.

At the bright end, the intrinsic scatter is relatively large due to the variation of the SEDs in the K_s band window and the selection of emitters with low-equivalent width may introduce spurious sources. We therefore introduce a further selection criterion using the rest-frame equivalent width, $EW_o > 50$ Å at $z = 2.49$. This corresponds to the $K_s - NB2288 = 0.55$ mag. The limiting Hα line flux of the emitter sample by these criteria is roughly 7.5×10^{-17} erg s^{-1} cm^{-2}. These values were computed using the same formula as used in Geach et al. (2008).

We found 12 objects that satisfy the selection criteria set here. After removing one object that was found to be a diffraction spike by visual inspection, the remaining 11 objects were cataloged as robust emission-line objects for further analysis. We note that the brightest object in the emitter sample is 4C 23.56. The observational properties of the emitter sample are summarized in table 1.

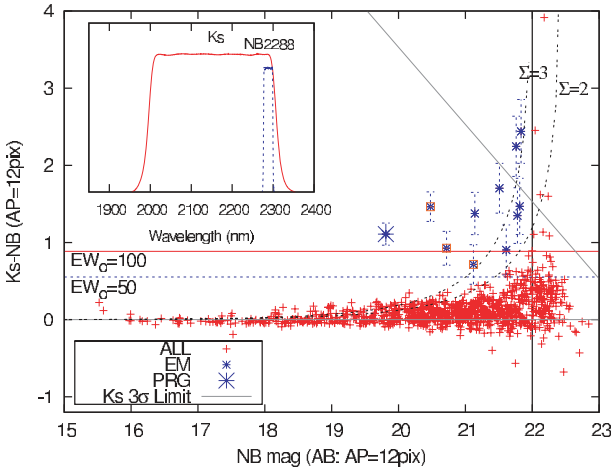

Fig. 2. $K_s - NB$ versus *NB* color–magnitude diagram for our cataloged objects (plus with the label "ALL"). The blue asterisks (labeled as "*EM*") indicate our selected emission-line objects based on the criteria $EW_o > 50$ Å, the narrowband aperture magnitude of less than 22 mag, and $\Sigma > 2$, which is used for analysis in the paper (one spurious object in the sample is removed here). The brightest emitter is 4C 23.56, which is indicated by a large asterisk. Emitters with red open boxes are the objects with MOIRCS spectra (except 4C 23.56). The tilted 4-dashed line indicates the 3-σ limiting magnitude of $K_s = 23.5$. The inset shows the transmission curve of the filters used in this study.

3.1.1. Spectroscopy

Though spectroscopic observations for all the emitter candidates have not yet been obtained, four of the 11 emission-line candidates have NIR spectroscopy. These data were taken before acquisition of the current *NB* data. The one- and two-dimensional spectra for each target are shown in figures 3 and 4. HAE #491 is the radio galaxy 4C 23.56, itself.

Due to the relatively low signal-to-noise ratio (*SNR*) of the spectroscopy, unambiguous identification of Hα via detection of the nearby [N II] or [S II] lines is only possible for the radio galaxy. The objects HAE #526 and HAE #153 are relatively bright, and we can say this is not [O III] λ5007 emission at $z = 3.571$ because of a lack of the [O III] λ4959 near 2.267 μm (as well as the lack of Hβ at 2.222 μm). Furthermore, the spectra of the latter object seems to have a hint of the broad component, which would not appear if it is [O III]. The lines from these two sources may also be from the Paschen series. If it is the Paα (Paβ) line, Paβ (Paγ) will be observed at 1.56 (1.95) μm. Unfortunately our spectra do not cover wavelengths below 2 μm. We have to make use of other information to exclude the latter possibility (see next section). For the object #354, the Hα signal at 2.288 μm is quite uncertain. However, we see a possible signal at 2.342 μm at the expected position of the [S II] line. Though both lines are quite low *SNR*, the inferred large [S II]/(Hα + [N II]) ratio of ~ 1 would indicate that the object harbours an AGN (Osterbrock 1989). We list the measured redshift values in table 1, supposing the line is Hα.

The velocity difference among these emitters is relatively small. They lie in the range of 2.287–2.289 μm (230 km s^{-1} range), which is in the red edge of the INGRID narrowband

[4] ⟨http://ssc.spitzer.caltech.edu/dataanalysistools/tools/mopex/⟩.

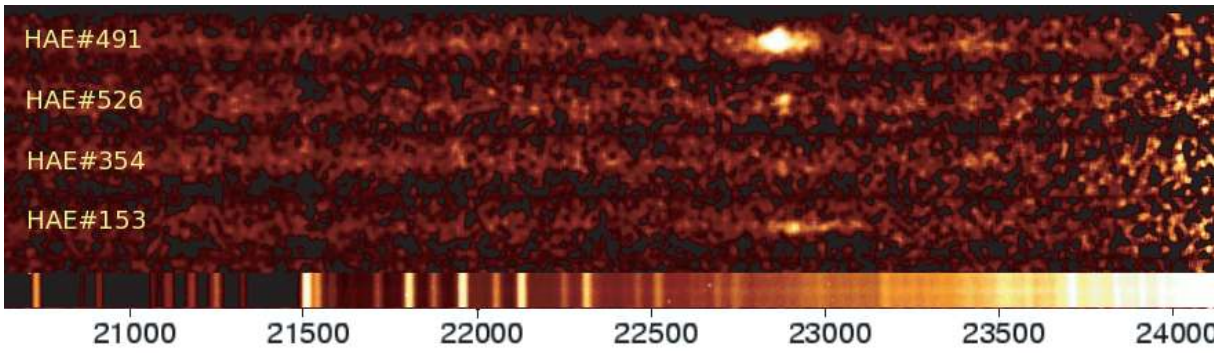

Fig. 3. MOIRCS MOS spectra of four Hα emitters. The top spectra (HAE #491) is 4C 23.56. The barcode-like pattern at the bottom is the OH airgrow spectra. The numbers at the bottom are wavelengths in angstrom.

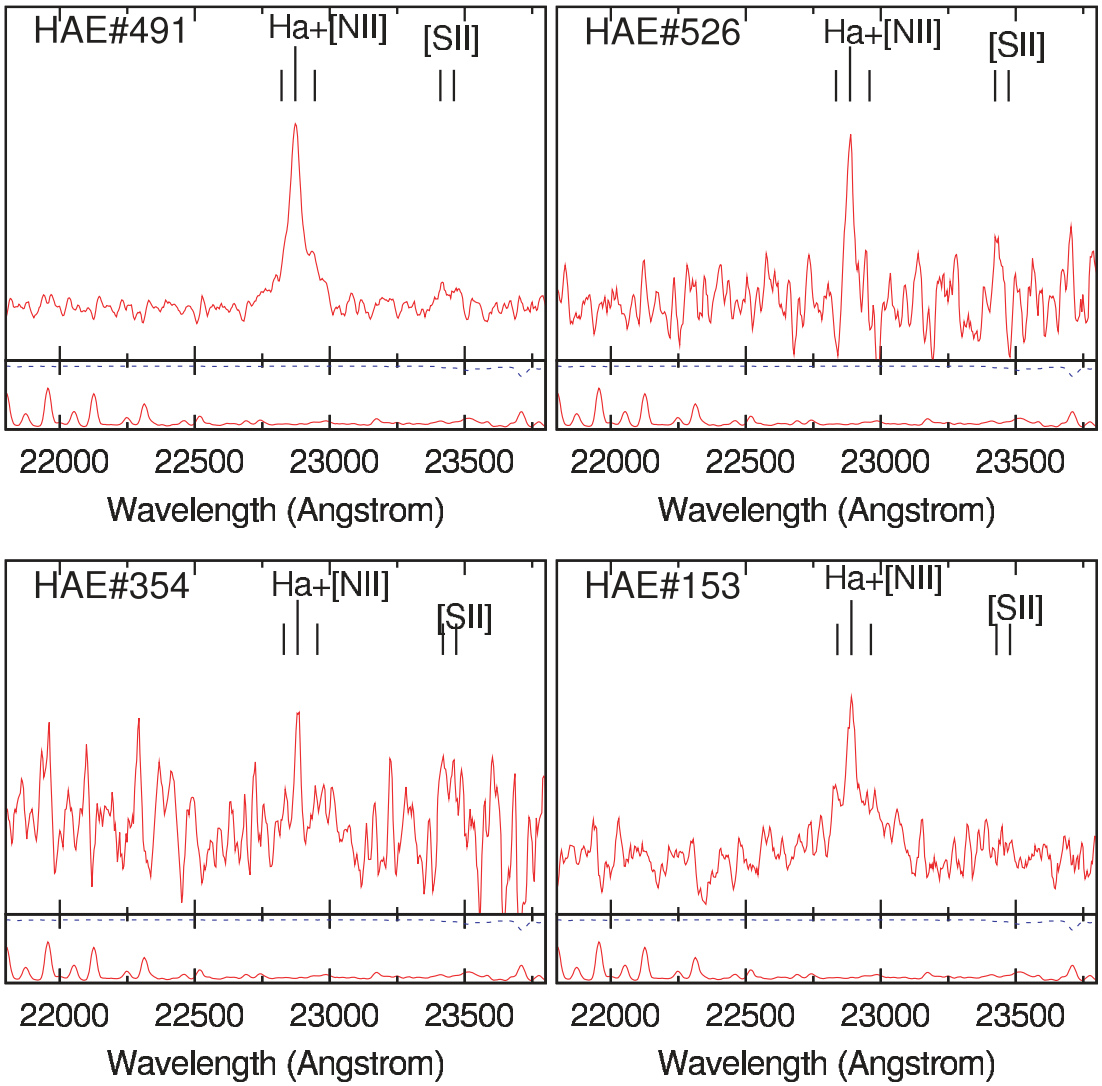

Fig. 4. MOIRCS MOS spectra of four Hα emitters. The top left spectra (HAE #491) is 4C 23.56. The OH airglow lines (red solid line) and the atmospheric transmission curve (blue dotted) are also plotted at the bottom panel of each spectra. Note that the spectra are not calibrated.

Table 1. Observational properties of candidate Hα emitters.

HAE ID	RA(J2000)	Dec(J2000)	K_s*	EW_o†	F(Hα)‡	F(24 μm)§	Redshift‖
153	21:07:16.96	23:30:30.5	21.82±0.07	327	3.64±0.77	78.9	2.4879
354	21:07:21.03	23:31:13.9	21.23±0.05	105	2.47±0.76	134.9	2.4865
356	21:07:15.70	23:31:11.9	22.78±0.12	282	1.35±0.50	125.9	—
393#	21:07:21.48	23:31:19.5	21.72±0.06	51	0.81±0.55	42.4	—
431	21:07:15.93	23:31:27.5	22.17±0.08	221	1.96±0.62	156.6	—
479††	21:07:21.63	23:31:41.2	22.37±0.08	956	4.25±0.72	131.8	—
491**	21:07:14.80	23:31:45.1	19.49±0.02	122	13.95	4630	2.4852
500††	21:07:21.84	23:31:41.8	>23.5	>780	>0.8	—	—
511††	21:07:22.58	23:31:43.4	22.98±0.12	300	1.18±0.46	156.5	—
526††	21:07:21.78	23:31:49.6	20.76±0.04	95	3.45±0.94	119.2	2.4872
543	21:07:17.61	23:31:50.5	>23.5	>505	>0.8	—	—

* The SExtractor MAG_AUTO output in AB mag.
† Rest-frame equivalent width based on the ($K_s - NB2288$) values by MAG_AUTO output.
‡ Continuum subtracted narrowband flux in 10^{-16} erg s^{-1} cm^{-2}.
§ Spitzer MIPS 24 μm flux in μJy from the DAOPHOT photometry.
‖ See subsection 3.1.
A possible low redshift interloper based on the *BJK* criterion (subsection 3.1).
** 4C 23.56. Its K_s magnitude is uncertain due to stray light (see subsection 2.1).
†† Galaxies in the "Eastern Clump" (figure 7; see subsection 3.3).

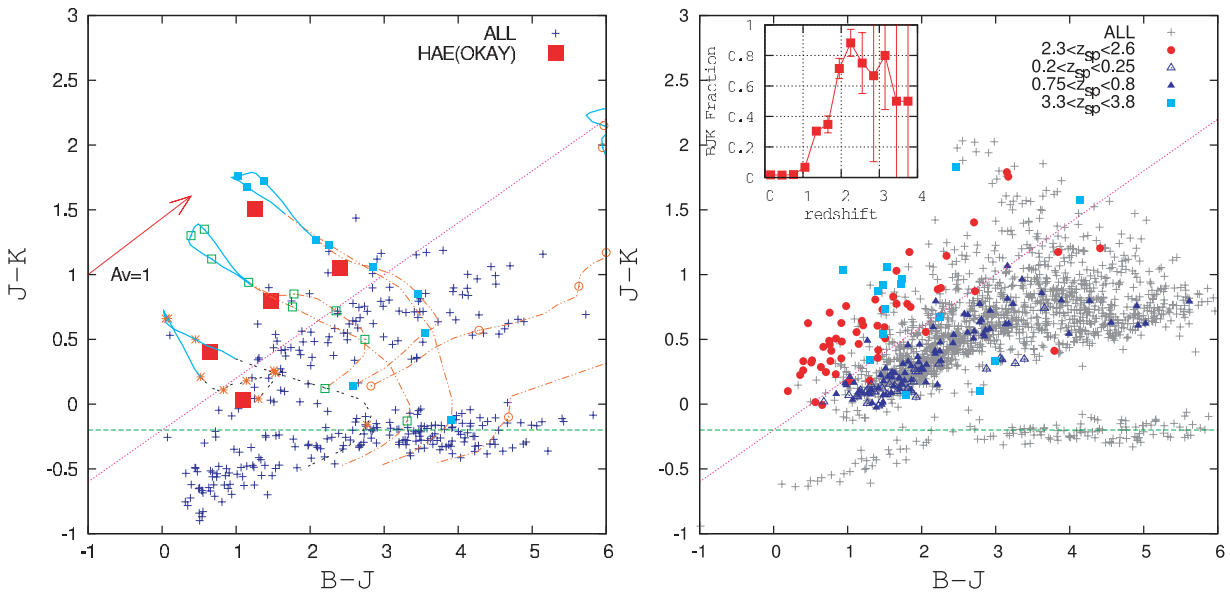

Fig. 5. (a: left) The $B-J$ versus $J-K_s$ two-color diagram for objects in the INGRID subfield. Five red boxes with the label "HAE (OKAY)" indicate the HAE candidates for which we can measure colors. Small plus symbols indicate other *NB*-selected objects in the area. The overplotted model tracks from blue to red indicate the "pure disk" model with continuous *SFR* (bluest), "50% disk + 50% bulge", "20% disk + 80% bulge", "pure bulge" (reddest, and mostly out of the figure) models, respectively. The cyan-colored region on each model track indicates the range $2.0 < z < 3.8$, and the farthest point in each cyan-colored track is around $z = 2.5$ to 3. See text for more details. (b: right) The same figure for galaxies in GOODS-North field (see appendix for details). The data is from the MOIRCS Deep Survey (MODS) Catalog with $K_s < 23$ mag (Kajisawa et al. 2009, 2011). In the figure, red filled circles indicate objects with spectroscopic redshifts of $2.3 < z < 2.6$, similar redshifts to our Hα emitters at $z \sim 2.5$. Blue triangles indicate objects at $0.2 < z < 0.25$ (open) as well as $0.75 < z < 0.8$ (filled), each of which corresponds to the redshift range for our foreground Paschen series (Paα and Paβ, respectively) interlopers, and the filled boxes (skyblue) indicate objects at $3.3 < z < 3.8$ to which the background [O III] emitter contaminant for our data would belong. Inset histogram shows the fraction of objects with known spectroscopic redshift that satisfy the *BJK* criteria we used here as the object selection at $z > 2$. Note that there is a very limited number of spectroscopically confirmed galaxies at $z > 2.7$, as indicated by the large $N^{1/2}$ errorbars.

filter function we used for pre-selection (2.25–2.29 μm). If these emission lines are not Hα, but from the interlopers unrelated to 4C 23.56, we can expect a more scattered distribution in wavelength range across the INGRID filter function. This is a strong indication that they are physically associated with both each other and 4C 23.56.

3.1.2. Broadband colors of HAEs

Our emission-line survey for Hα at $z = 2.49$ may contain interlopers at different redshifts. As we showed in the previous section, the spectroscopic detection of a single line remains

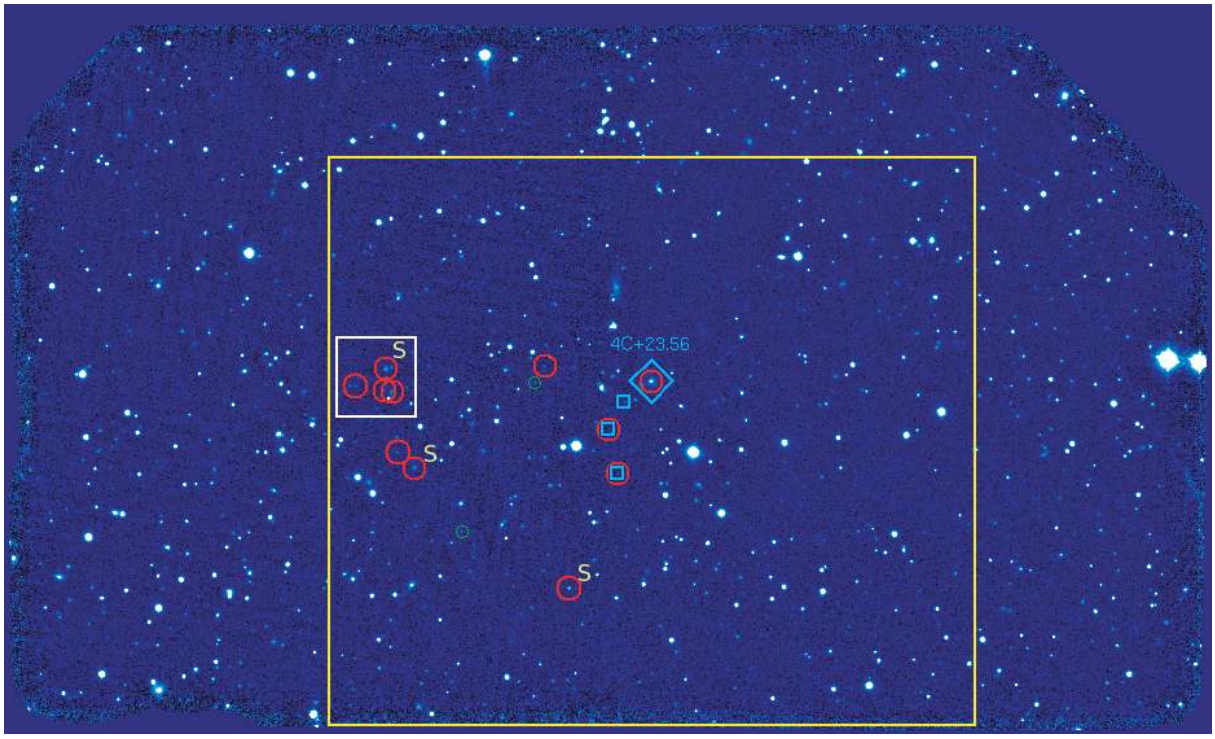

Fig. 6. Distribution of the HAEs on the *NB2288* image. The FOV covers $7' \times 4'$ on the sky, with north and east to the top and left, respectively. The red open circles indicate the candidate HAEs by our selection. The three small open boxes indicate the Distant Red Galaxies from Kajisawa et al. (2006b) that show emission-line excess ($K_s - NB > 1$) as seen in figure 13 (also see appendix 2). Two of them are also identified as HAEs. The remaining one is the only *NB*-excess object among the ERO sample by KC97. Two small open circles (green) indicate the candidate emission-line objects that satisfy the criteria of $\Sigma > 2$ but are fainter than $NB = 22.0$. Three red open circles with the letter "S" indicate the emitters with the MOIRCS spectra (sub-subsection 3.1.1). 4C 23.56 is shown as a large diamond. The area enclosed by a white box indicates the same area as shown in figure 7. The yellow rectangular region indicates the INGRID subfield (see subsection 3.1).

ambiguous; it could be Paα for example. Geach et al. (2008) used color selection as well as photometric redshifts to distinguish interlopers in their Hα emitter sample at $z = 2.2$. They estimated that, among their 55 "robust" sample galaxies, a third can be lines other than Hα (12 Paα, 6 Paβ, and one [O III]). Their result indicates that foreground objects (Paα objects at $z = 0.22$ and Paβ objects at $z = 0.78$) could be the major contaminants of our data.

To make sure that our detected emission-line objects are mainly Hα emitters, we measured the continuum color of our emission-line candidates using our supplementary Subaru B-band and WHT J-band data (subsection 2.4). The J-band data cover the central $3\farcm8 \times 3\farcm4$ area of the MOIRCS field of view (here we refer to the area as the "INGRID subfield", as shown in figure 6), while the whole area is covered by B-band data.

Though our selected emission-line candidates all lie in the INGRID subfield, 4 objects are not seen in our B-band data. Two more objects are overwhelmed by the PSF of bright nearby stars. We could measure a *BJK* color for five objects. Fortunately, all four spectroscopic targets are in this sub-sample. A $B - J$ versus $J - K_s$ two-color diagram is shown in figure 5a. The Hα emitter candidates are marked by filled boxes (red).

As discussed in detail in appendix 1, the $B-J$ versus $J-K_s$ two-color diagram is found to be quite effective for rejecting objects at $z < 1$. Figure 5b is the *BJK* two-color distribution of galaxies in GOODS-North region from the MOIRCS Deep Survey (Kajisawa et al. 2009, 2010, and references therein). The objects that satisfy $(J - K_s) > 0.4\ (B - J) - 0.2$ are empirically shown to have a spectroscopic redshift of $z > 1$ from figure 5b.

The position of our 5 emission-line objects in figure 5a is quite favorable; with the exception of one object, they satisfy the *BJK* criterion. These 4 *BJK* emitters comprise our spectroscopic sample. Thus, we can conclude that the emission line we detect spectroscopically is indeed Hα, not from the Paschen series. This is strong support for the existence of a protocluster at $z = 2.5$ in the 4C 23.56 field.

One object whose color is below the *BJK* line could be an interloper, though we cannot conclude this for certain until its spectra is obtained. One such object can be expected from the field survey, as we can see in subsection 4.1. During the following discussion we consider that all our selected emission-line objects are HAEs at $z \sim 2.49$, though a few of them might be foreground objects.

3.2. *Spatial Distribution of HAEs*

The spatial distribution of our HAE sample on the sky is displayed in figure 6. The position of 4C 23.56 is marked with a large diamond. The distribution of our selected HAEs (shown with open red circles) is quite tightly clustered at the east to south-eastern side of the radio galaxy.

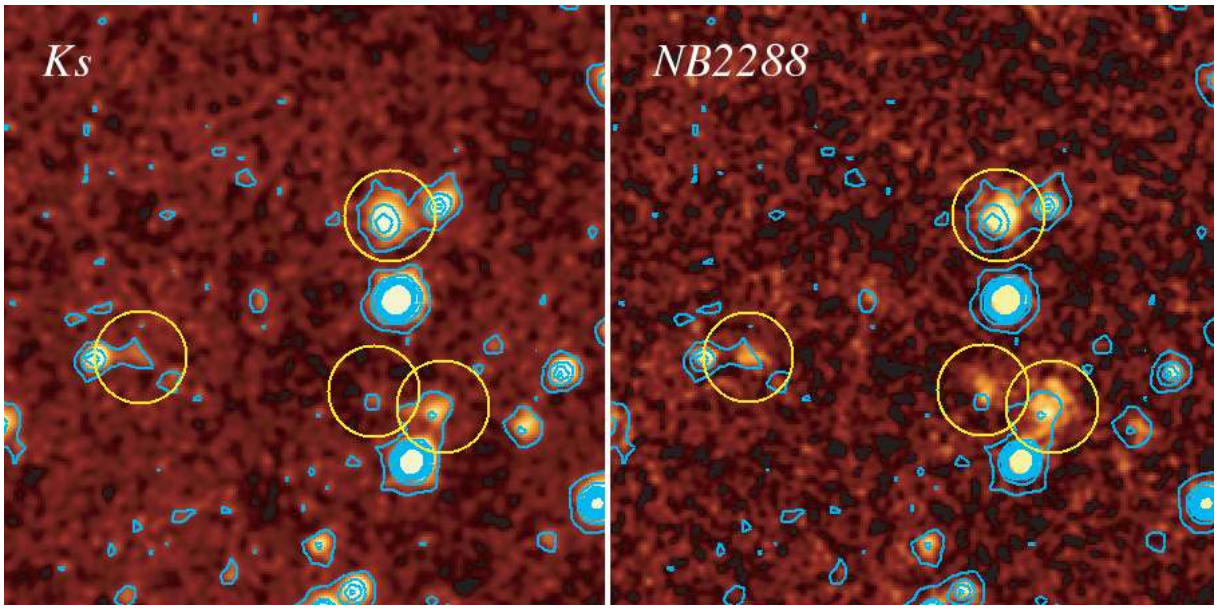

Fig. 7. Zoom-up views of the "Eastern clump" region in both the *NB2288* (right) and the K_s (left) images. The objects at the center of each yellow circle represent the HAEs. The 1σ, 4σ, 7σ, 10σ, and 13σ contours based on the rms noise of the K_s image before smoothing is applied to the Gaussian-smoothed K_s images, and is also overlaid on the *NB2288* image. A clear extended or offset light distribution of HAEs in the *NB2288* image is seen for (at least) the three objects on the right. Interestingly, the directions of the offset light distributions for these three objects are roughly the same (to the North-West). The size of the area is about $26'' \times 26''$ ($\sim$0.5 Mpc $\times$ 0.5 Mpc comoving).

The biased distribution of HAEs to the eastern (i.e., channel-1) side of 4C 23.56 is not due to the wavelength shift of the filter transmission window or any difference between channels. It is also not due to some unexpected trouble in the channel-2 filter, because 4C 23.56 and the adjacent two emitters are actually detected on the channel-2 side. The inhomogeneous distribution seems to be the reflection of the real distribution of the emitters.

If we suppose that the majority of the protocluster members are strongly redshifted relative to 4C 23.56, the situation could change. As discussed in sub-subsection 2.1.1, HAEs redshifted by $> 1000\,\mathrm{km\,s^{-1}}$ relative to 4C 23.56 will drop off from our detection window in the outer half of the FOV. In the inner half of the FOV we should detect objects with large velocity differences. Though our three HAEs with spectroscopic redshift have small velocity offset ($< 230\,\mathrm{km\,s^{-1}}$), further spectroscopy for all of the HAEs may uncover a biased velocity distribution.

3.3. Offset Hα Emission in the "Eastern Clump"

Here, we comment on objects in the area enclosed by a small white box in figure 6. There is a group of 4 emitters that lie within a $15''$-diameter area ($=$ 300 kpc comoving), which is also shown in figure 7 as a zoomed view. We call this area the "Eastern Clump". The compact size of the HAE group suggests that they might eventually merge into one massive galaxy in the future and become (one of) the brightest cluster member(s).

One notable character of HAEs in the Eastern Clump is that the light distribution of each HAE in the *NB2288* image is offset from the K-band object position, as shown in figure 7. Especially interesting is that the offset direction of emission-line gas in three HAEs on the west side of the clump in figure 7 is roughly aligned to the North to North West.

To show these offsets more clearly, we ran SExtractor on each image independently and measured the positional offset of objects detected in both images. The result is shown in figure 8. In the figure, the 1-, 2-, and 3-σ scatter, based on objects that have similar magnitudes to the HAEs (dots), are shown by circles of dashed lines. The HAEs are marked as filled squares, with the objects in the Eastern Clump shown in figure 7 overlaid with asterisks. There are two more large-offset ($> 3\sigma$) objects seen in figure 8. One of them is indeed the object just south of the Eastern Clump. We confirmed that the offset of the emission-line gas is not due to a poor astrometric alignment of the two images; all of the other objects adjacent to the Eastern Clump show the same scatter shown as dots here.

The K-band light centroid can be considered to be the center-of-mass for each galaxy. Therefore, these offsets of the Hα emission indicate that star-formation is occurring at the periphery of the galaxies. This could be due to interactions among the galaxies triggering star-formation (e.g., Sulentic et al. 2001; Cortese et al. 2006), though the apparent alignment of the offset direction is difficult to explain. The apparent offset of the Hα emission is roughly $0\farcs2$–$0\farcs4$, corresponding to a physical size of 1.6–3.2 kpc at $z = 2.49$.

Another possible explanation may be that vast outflows of emission-line gas are being launched from these galaxies. The direction of such outflows could be influenced by the direction that the group is moving towards the center of the cluster potential. If the cluster potential is already filled by dense intracluster gas, the expelled emission-line gas from these galaxies may leave a "wake" behind each galaxy. In the local universe, similarly offset light from emission-line gas is caused by ram-pressure stripping of galaxies by intracluster gas (e.g., Yoshida et al. 2002; Yagi et al. 2007; Sun et al. 2007). For example,

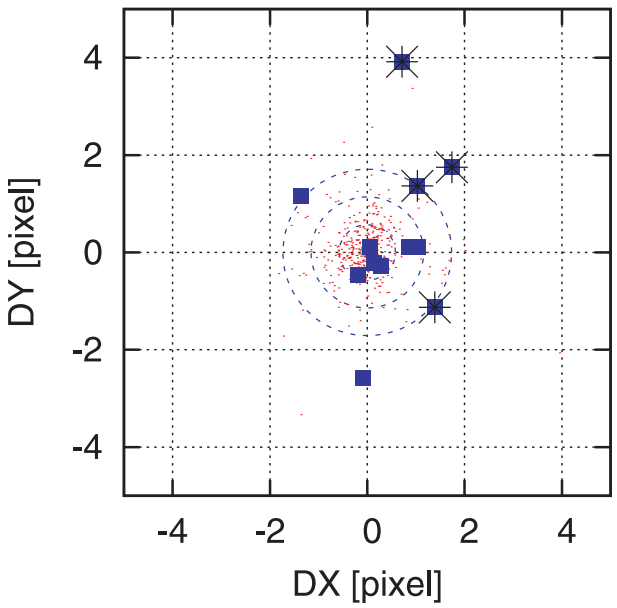

Fig. 8. Difference of the object position between the K_s and the *NB2288* images. Objects that have similar magnitudes to our HAEs are used (dots). The 1-, 2-, and 3-σ scatter of the distribution are shown as dashed circles in the figure from the inner to outer, respectively. The result for the HAEs is shown by filled squares, with the 4 HAEs in Eastern Clump in figure 7 overlaid by asterisks. The offset is shown in X and Y pixel coordinates, where the MOIRCS pixel scale is $0\farcs117$/pixel (corresponding physical scale is 0.96 kpc/pixel at $z = 2.48$).

Cortese et al. (2007) discovered a trail of blue emission-line knots behind an object in Abell 2667 at $z = 0.23$. Our detected offset of the Hα emission in the Eastern Clump may be similar.

The detection of extended X-ray emission from 4C 23.56 intracluster gas is the key for falsifying the ram-pressure stripping scenario. The field was observed by XMM and reported by Johnson et al. (2007). Though they detected extended soft X-ray emission near the radio galaxy in a $\sim$30 ks EPIC exposure, they concluded that inverse-Compton scattering of CMB photons is the most likely emission mechanism. Indeed the position and direction of the X-ray extension is well aligned with the radio lobe, which extends $\sim$0.5 Mpc north-east/south-west from the radio galaxy, and not with the direction where the Eastern Clump lies. For now, there is no evidence of thermal X-ray emission from hot intracluster gas.

3.4. HAEs and the Spitzer MIPS Data

Spitzer MIPS 24 μm imaging has been used to probe star-formation activity at $z \sim 2$ (e.g., Daddi et al. 2007). There is public, archived deep 24 μm MIPS data for the 4C 23.56 field (subsection 2.4). If the protocluster around 4C 23.56 is characterized by active star formation, we may also see it as an excess of faint MIPS sources.

In figure 9 we show our re-processed MIPS 24 μm image. The strong point source at the center of the image is 4C 23.56. We can clearly see an excess of faint MIPS sources around the radio galaxy compared to the outer parts of the image. We also find that 9 objects out of our 11 HAE sample (shown as red open circles) have MIPS counterparts. However, the apparent excess of 24 μm sources does not seem to be due solely to the HAE counterparts. Here, we examine the excess of MIPS-selected objects in the 4C 23.56 field. The 24 μm photometry and the inferred star-formation rates for the HAE counterparts are separately discussed in the next section (subsection 3.5).

To estimate the density excess of MIPS sources quantitatively, we have to consider the difference of the exposure coverage across the field. We first exclude any area that has an exposure time less than 1/3 of the total integration. We then set the SExtractor object detection threshold to 2.8σ. This is higher than usual, so that the detection is not affected by the S/N difference due to the variation of the exposure time across the field. To check the robustness of the detection threshold further, we reversed the pixel count of the MIPS image, and executed object detection with the same SExtractor parameters. Besides a clear pixel defect, we detected no sources in the inverse image, indicating that the no fake object from the sky variation was included in the current analysis. Furthermore, we exclude all objects with a flux density less than 90 μJy, since they may suffer from source confusion in crowded regions.

We also introduced an upper flux density cut of 275 μJy, because most of our HAEs were fainter than 200 μJy. Any object much brighter than 200 μJy has a high possibility of being in the foreground. The upper flux-density cut was chosen to be roughly twice the median 24 μm flux density of our HAEs.

Note that we applied SExtractor detection directly to the 24 μm data for the source-density excess estimate. For the *SFR* estimate from the MIPS photometry for our HAE sample, we used DAOPHOT software, as described in subsection 2.4, because it could provide a more robust flux estimate of each source.

The resulting density map of the faint (90–275 μJy) MIPS sources is overlaid on figure 9 as contours. The distribution of sources has been smoothed by a Gaussian kernel of $\sigma = 30''$. For reference, the position of the HAEs are shown as red open circles. It is quite clear that the MIPS source density excess closely matches the HAE distribution.

To quantify the density excess of MIPS sources further, we defined the "excess region" as the 80″-radius region around the peak density contour, and compared the excess within the region with the "outer region" at larger radii. From the density of faint MIPS sources in the "outer region", we estimated the expected number in the "excess region" as being 15.3. On the other hand, we counted 39 objects in the "excess region", yielding a number enhancement of $2.55^{+0.59}_{-0.48}$. This corresponds to a 4.5-σ excess by proper Poisson statistics (Gehrels 1986). As a crosscheck, we downloaded deep MIPS data for GOODS-N/S fields[5] and counted sources in the same manner, yielding the expected count of 18.2 ± 0.7 for an area with the size of the "excess region". The source counts of deep MIPS data for ELAIS-N1 field by Chary et al. (2004) also show the expected number of 17.0. Our number is consistent with those surveys, considering the uncertainty by the cosmic variation.

The HAEs with MIPS counterparts (9) can only explain less than half of the total excess count ($\sim$24). This implies

[5] The data is available in ⟨http://ssc.spitzer.caltech.edu/spitzermission/observingprograms/legacy/goods/⟩.

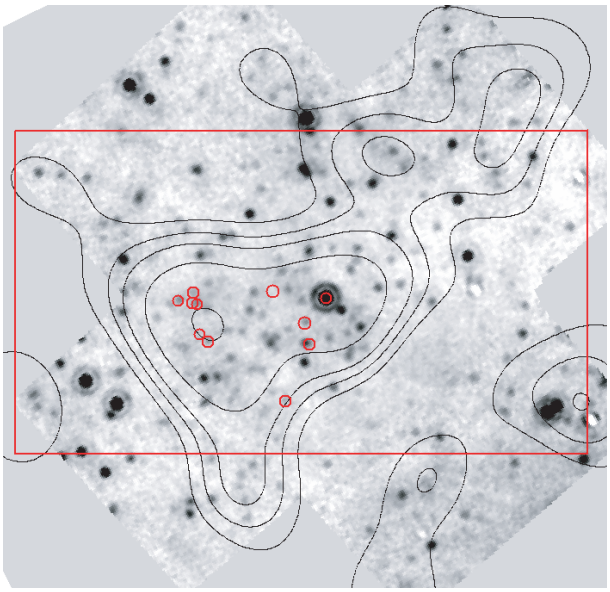

Fig. 9. Density contour of the faint Spitzer MIPS 24 μm sources is overlaid on the MIPS 24 μm image. The area with an exposure coverage less than 1/3 of the total is not shown here. The brightest source in the center is 4C 23.56. The red rectangular region indicates the MOIRCS field of view (North is up: see figure 6), and the red open circles indicate the HAEs. The distribution of the faint MIPS sources ($90 < F_{24\mu m}$ [μJy] < 275) is smoothed with a Gaussian kernel with $\sigma = 30''$, and shown as contours. The contour interval is $(2i + 1)$-times ($i = 0, 1, 3, 6, 11$) the square root of the average MIPS source density (from the "outer region": see text) above average.

that our shallow Hα emitter survey may be missing an even larger number of the dust-enshrouded star-forming objects in the excess region. Future follow-up observations using ALMA etc would be quite interesting to understand these hidden dusty sources.

3.5. *Star-Formation Rate and Stellar Mass of HAEs*

In this section we estimate the star-formation rate (*SFR*) and the stellar mass of our HAE sample. We note, however, that the estimation of the *SFR*s and the stellar masses for our HAE sample is uncertain and should be treated with caution.

3.5.1. *Hα-based star-formation rate of HAEs*

It is known that dust absorption lowers the measured *SFR* from Hα emission relative to the intrinsic *SFR* based on radio or FIR emission (e.g., Hopkins et al. 2001; Afonso et al. 2003; Erb et al. 2006; Daddi et al. 2007). The contamination of the [N II] 6583 Å emission line to the narrowband flux is also an unknown factor (here we set the factor as 0.2). The contribution of AGN to the ionizing radiation also adds uncertainty to the estimate. These uncertainties can be calibrated using future deep spectroscopy of complete HAE samples.

Kennicutt (1998) gives the conversion formula from L(Hα) to the *SFR* as

$$SFR\ (M_\odot\ \mathrm{yr}^{-1}) = 7.9 \times 10^{-42}\ L(\mathrm{H}\alpha)\ (\mathrm{erg\ s}^{-1}). \quad (2)$$

Though the conversion assumes the standard Salpeter (1955) Initial Mass Function (IMF), the IMF is known to overestimate the stellar mass. We used the conversion correction for the Chabrier (2003) IMF by dividing the value by 1.7, for mainly practical reasons, so that our data could be compared to some recent Hα-based *SFR* estimates in the literature. Note that the dust extinction should affect the *SFR* estimate much more than the uncertainty due to [N II] contamination. An AGN contribution can also exist for some galaxies; the unusually high derived *SFR* for 4C 23.56 is clearly due to the AGN contribution to the Hα flux.

As for the extinction-correction factor, the *BJK* diagram (figure 5a) is a useful diagnostic for a part of our sample. In the figure we show the $A_V = 1$ extinction vector using the Calzetti (2001) extinction law. Assuming that the objects are pure disks with dust extinction, the color distribution of the HAEs indicates that the level of the extinction ranges from 0 to $\sim$1. Using the Calzetti (2001) recipe and the conversion of $A_{\mathrm{H}\alpha} = 0.82\,A_V$, an extinction correction factor of 1 to 5 is estimated.

For the remaining 6 objects we cannot estimate the extinction. For a comparison, the recent study by Onodera et al. (2010) estimated the level of extinction for their sBzK-selected Hα emission-line objects, which seem to have roughly similar stellar masses as our HAEs (sub-subsection 3.5.3). Their extinction estimate is based on an SED fitting with additional correction, as prescribed by Cid Fernandes et al. (2005) and Savaglio et al. (2005). Their table 4 indicates that the average of the extinction correction factor is 4.9. We applied correction factors of 4.9 for the objects for which we could not use the *BJK* diagram. The raw and the extinction-corrected *SFR* for each HAE are listed in table 2.

3.5.2. *Spitzer MIPS star-formation rates*

The bolometric infrared luminosity of galaxies correlates very well with other measures of the star-formation rate, and may be the most robust measurement of the *SFR*. The infrared light is emitted by dust-reprocessing of the emitted UV light from young stars, and therefore peaks at rest-frame wavelengths between 100 and 300 μm. In lieu of observations at these frequencies, the longest wavelength datapoints need to be extrapolated using assumed SED models. For this radio galaxy field we used the observed 24 μm imaging to infer the *SFR*s for the discovered Hα emitters.

We used the SED template for Arp 220, a possible low-redshift analogue, to correct the 24 μm to rest-frame 8.0 μm luminosities (Rieke et al. 2009). From these values we estimated the bolometric infrared luminosity using the Chary and Elbaz (2001) and Dale and Helou (2002) SED models, following the prescription by Daddi et al. (2007).[6] The resulted infrared luminosities from the two SED models were averaged. Finally, we used the following Kennicutt (1998) L_{IR} to *SFR* conversion:

$$SFR\ (M_\odot\ \mathrm{yr}^{-1}) = 3.0 \times 10^{-44}\ L_{\mathrm{FIR}}\ (\mathrm{erg\ s}^{-1}). \quad (3)$$

Note that the original formula was divided by 1.5 for Chabrier (2003) IMF (Yoshikawa et al. 2010). These conversions and extrapolation result in *SFR*s, which are the uncertain by up to factors of a few (Papovich et al. 2007). For our purposes, to estimate the FIR output from likely protocluster galaxies, these uncertainties are tolerable. The Herschel Space Telescope

[6] The formula (4) in Daddi et al. (2007) has a possible typo. The constant should be +1.745, not +1.23, to match the description in the text and to reproduce the relation in their figure 7.

Table 2. The estimated basic properties of the Hα emitters.

HAE ID	$\log(M/M_\odot)$	$L_{\mathrm{H}\alpha}$*	$SFR^{\mathrm{raw}}_{\mathrm{H}\alpha}$	$SFR^{\mathrm{corr}\dagger}_{\mathrm{H}\alpha}$	$\log(L_{\mathrm{IR}}/L_\odot)$	$SFR(24\,\mu\mathrm{m})^\ddagger$
153	11.124 ± 0.235	14.4 ± 3.0	67.13	187.96	12.533	410
354	11.430 ± 0.225	9.75 ± 3.02	45.57	355.45	12.792	743
356	10.635 ± 0.260	5.34 ± 1.96	24.94	122.21	12.758	688
393	11.178 ± 0.230	3.19 ± 2.16	14.92	14.92	12.237	207
431	10.948 ± 0.243	7.74 ± 2.45	36.17	177.23	12.864	877
479	10.844 ± 0.240	16.75 ± 2.82	78.30	383.67	12.781	724
491§	< 12.320§	55.0 ± 6.8	257.15	1429.75‖	N/A#	N/A#
500	< 10.164	> 4.63	> 24.85	—	—	—
511	10.531 ± 0.262	4.65 ± 1.8	21.72	106.43	13.091	876
526	11.667 ± 0.220	13.6 ± 3.7	63.67	311.98	12.869	647
543	< 10.164	> 4.13	> 19.28	—	—	—

* Extinction-uncorrected values in units of 10^{42} erg s^{-1}.
† In $M_\odot$ yr^{-1}. See text for detail of the extinction correction.
‡ Spitzer MIPS 24 μm-based *SFR* in $M_\odot$ yr^{-1}.
§ 4C 23.56. Its mass estimate is unreliable due to the uncertainty in its K_{s} magnitude (see subsection 2.1). If we use the value by KC97, the estimated stellar mass is 11.67.
‖ Affected by an AGN contribution. The *SFR* value is quite uncertain.
Affected by an AGN contribution. The $L_{24\mu\mathrm{m}}$ conversion from the observed MIPS flux is impossible due to the limitation of the Chary and Elbaz (2001) model.

has already quantified these uncertainties for other fields (e.g., Rodighiero et al. 2010), and may eventually provide longer wavelength data for these and other protocluster galaxies. The results of the MIPS-based *SFR* is also listed in table 2.

The resulting MIPS-based *SFR*s are significantly (a factor 2–14 with median of 3.6) higher than the *SFR*s based on the extinciton-corrected Hα. We discuss this further in subsection 4.3.

3.5.3. Stellar mass of HAEs

Next we estimate the stellar mass of our HAE emitters. We employed the conversion formula for the stellar mass from the K_{s}-band photometry by Daddi et al. (2004). They showed that for galaxies at $1.4 < z < 2.5$ the stellar mass is reasonably estimated using

$$\log(M_*/10^{11}\,M_\odot) = -0.4\,(K^{\mathrm{tot}}_{\mathrm{Vega}} - K_{11}) + 0.218\,[(z-K)_{\mathrm{AB}} - 2.29], \quad (4)$$

where K_{11} is the K-band magnitude (Vega scale) of the average $10^{11}\,M_\odot$-mass objects of their sample (= 20.14 for the average redshift of $\langle z \rangle = 1.9$). Considering the difference in the luminosity distance between $\langle z \rangle = 1.9$ and 2.49, and the average distribution of $(z-K)_{\mathrm{AB}}$ color of 1 from the figure 7 of Daddi et al. (2004), we derived the estimate of the stellar mass at $z = 2.49$ as

$$\log(M_*/10^{11}\,M_\odot)_{2.49} = -0.4\,K^{\mathrm{tot}}_{\mathrm{AB}} + 8.8, \quad (5)$$

where $K^{\mathrm{tot}}_{\mathrm{AB}}$ is in AB-magnitude scale.

As a check of the validity of the formula, we compared it to the stellar mass estimates based on SED fitting the 12-band photometry for the GOODS-North MOIRCS Deep Survey Catalog (for details of the model fitting, see Kajisawa et al. 2009, 2011). Figure 10 shows the stellar mass versus K-band magnitude of the cataloged objects in the redshift range $2.3 < z < 2.6$, for objects with photometric redshifts (open boxes) and spectroscopic redshifts (crosses). Though the Daddi estimator by equation (4) fits the overall distribution of the photometric redshift sample reasonably well, the slope seems a bit shallower than the data. Therefore, we fit all of the photo-z-based data in figure 10, and obtained the best-fit line as

$$\log(M_*/10^{11}\,M_\odot)_{2.49} = -0.5127\,K^{\mathrm{tot}}_{\mathrm{AB}} + 11.312. \quad (6)$$

We used this formula for the conversion from K-band magnitude to the total stellar mass. The rms scatter of the fit was calculated, and found to be only 0.2 dex, consistent with the value quoted by Daddi et al. (2004) (but note that the scatter increases to 2.4 dex if we use brighter subsample of $K_{\mathrm{s}} < 23$). The resulting stellar mass for each HAE galaxy are listed in table 2. We note that the K_{s}-band magnitudes for HAEs will be affected by the Hα emission. The rest-frame equivalent width of 100 Å will affect the mass estimate by 11%. The median value of the offset due to line emission is ∼20%. This is small compared to the mass estimation uncertainty of > 0.2 dex. We also calculated the specific star-formation rate (*SSFR*) for the HAEs. The results are given in table 2.

4. Discussion

4.1. Comparison to Field Counts

Our discovery of 11 HAE candidates to a limiting flux of 7.5×10^{-17} erg s^{-1} cm^{-2} in 23.6 arcmin^2 area should be compared with the number expected in the general field. Geach et al. (2008) provided us with excellent reference data. Their HiZELS survey measured the number density of Hα emitters at $z = 2.23$ over 0.6 deg^2 using the narrow-band filter (H_2S1, $\lambda_{\mathrm{c}} = 2.121\,\mu$m, $\delta\lambda = 0.021\,\mu$m) to a line flux limit of 10^{-16} erg s^{-1} cm^{-2}. Their survey field is 91.5-times wider than our own, and their filter has a similar bandwidth to our *NB2288* filter. They detected 180 emitters including non-Hα (e.g., Paschen series, [Fe II], [O III]) objects under their selection criteria of *observed EW* of 50 Å (= 14.3 Å in rest frame at $z = 2.5$). Since our data are deeper than theirs, we set our detection limit to match theirs. To an *NB* magnitude of

21.3 mag we found 5 emitters. Next we had to estimate how many of their 180 emitters would satisfy our threshold of *rest-frame EW* of 50 Å. In the filter bandwidth they used, the rest-frame EW_o of 50 Å (at $z = 2.49$) corresponds to a narrow-band excess of 0.56. We estimated the number of emitters that satisfy the $EW_o > 50$ Å to be about 90 from their figure 1. Scaling the number to match our field of view, we derived the expected number of the *field* emitters in our field to be ~ 1. Note that, similar to our sample of HAE candidates, this field count includes interlopers too. Considering our total of 5 emitters, we can say that our field contains 5-times the expected field count.

Recently, Geach et al. (2010) published more generalized HAE counts from their HiZELS and other surveys. Their table 2 gives the expected field HAE number counts at the limit of 1×10^{-16} erg s^{-1} cm^{-2} ($EW_o > 10$ Å) to $z = 2.2$. Extrapolating their result to $z = 2.5$ by a third-order polynominal and applying our survey size, we obtained the expected field count in our survey area as $1.2^{+0.63}_{-0.46}$. If we again suppose that roughly half of them can be observed as HAE in our *EW* cut of $EW_o > 50$ Å, the expected field count could be only 0.6. Thus, the result suggests the overdensity even more strongly.

A deep and wide narrowband HAE survey using the new instrument HAWK-I was recently published (Hayes et al. 2010a). A field of 7.′5 × 7.′5 in GOODS South was surveyed using the narrowband filter *NB2090* ($\lambda_c = 2.095\,\mu$m, $\delta\lambda = 0.019\,\mu$m). Their data are extremely deep, with a 5 σ limiting magnitude of 24.6 AB, corresponding to a line flux limit of 6.8×10^{-18} erg s^{-1} cm^{-2}, nearly an order of magnitude deeper than our own data. The inset histogram in their figure 1 shows that the number of emitters they detected at $NB < 22$ is 9, under their *EW* cut of $EW_o > 20$ Å (corresponding to the emission-line excess of 0.29). In their filter bandwidth our selection criterion of $EW_o > 50$ Å corresponds to an emission-line excess of 0.60 mag. We estimate that 5 of their emitters satisfy our selection criterion of $EW_o > 50$ Å from their figure 1. Considering the difference in survey areas, the expected field count of the *NB* emitters for our data is estimated to be 2.5 ± 1. This estimate is consistent with the results from another deep survey, carried out on a smaller field, by Moorwood et al. (2000). Our count of 11 HAEs is therefore $5.3^{+5.3}_{-2.6}$ times (or 3 σ) more than the field count, which is based on a proper treatment of the small number Poisson statistics by Gehrels (1986).

We note that the redshift evolution of the HAE number count suggested by Geach et al. (2010) is quite strong: extrapolating from redshifts below $z = 2.2$ to $z = 2.5$, the predicted number counts of HAEs with flux larger than 1×10^{-16} erg s^{-1} cm^{-2} decreases by 60%, from 8582 to $\sim 5380\,\mathrm{deg}^{-2}\,z^{-1}$. Although the evolution in the number density depends on the limiting flux, this correction for the difference in redshifts (from $z = 2.2$ to 2.5) will also reduce our field count estimate based on Hayes et al. (2010). Our estimate of the overdensity of a factor 5 should therefore be considered to be conservative.

As we show in table 2, about half of our HAEs seem to have a stellar mass of $\gtrsim 10^{11}\,M_\odot$. Such massive objects at $z \sim 2.5$ are relatively rare in the field. For example, if we count such objects using the MODS catalog (sub-subsection 3.5.3), we find only 10 in their 103-arcmin^2 survey area at $2.3 < z < 2.6$ (figure 10). By scaling the value to our survey area of 23.6 arcmin^2 and $2.47 < z < 2.49$, we estimate the expected number in our FOV to be 0.15. The excess of such massive galaxies in the 4C 23.56 field is clear. Recalling that these massive galaxies in the 4C 23.56 field are Hα-selected, there could be more inactive massive galaxies missed by our search. We are planning to execute multi-wavelength observations of the 4C 23.56 field. The data will help identify such inactive massive galaxies, and will reveal the whole picture of the protocluster.

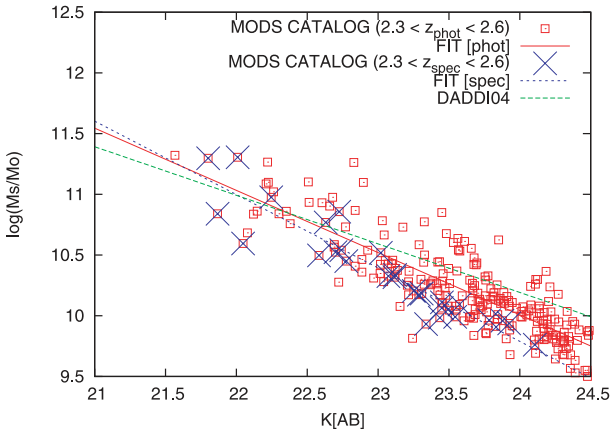

Fig. 10. K_s versus stellar mass relation for objects at $2.3 < z < 2.6$ from the MOIRCS Deep Survey (MODS) catalog used in Kajisawa et al. (2009). The catalog includes a compilation of the spectroscopic redshift data published, and are shown as crosses in the figure. The stellar mass is based on the SED-fitting by the 12-band photometry from UV to infrared, with the SED model from Bruzual and Charlot (2003). Details of the model fitting procedure can be found in Kajisawa et al. (2009).

4.2. *Comparison with Other Protoclusters*

Although there are several known protoclusters at $z > 2$, there is only one other field that has been searched for HAEs. Kurk et al. (2004a) searched for HAEs in their discovered protocluster surrounding PKS 1138−262 at $z = 2.16$. Here we compare the number of detected HAEs.

According to their figure 6 and table 5, their selection of $EW_o > 50$ Å and $\Sigma > 3$ combined with a magnitude limit of $NB_{\mathrm{Vega}} < 20.2$ would match the selection we use here. There are ~ 10 HAEs meeting these criteria in the PKS 1138−262 field, roughly the same number as the 4C 23.56 field. Their HAE survey field is roughly half of ours (but wider than our "INGRID subfield" where all our HAEs lie). However, if we use the distribution of their Ly α emitters as a proxy for the HAE distribution (their figure 10) there would be at most an additional two HAEs. This implies that the richnesses of the 4C 23.56 and the PKS 1138−262 fields are likely comparable.

There are differences in the properties of the HAEs in the PKS 1138−262 and the 4C 23.56 protoclusters, primarily the spatial distribution of the HAEs relative to the radio galaxies. In the PKS 1138−262 system the HAEs are rather homogeneously distributed around the radio galaxy, with some evidence for higher surface density closer to it. In the 4C 23.56 field the radio galaxy lies at the western edge of the HAE distribution. This does not appear to be a result of any observational

bias, as described in sub-subsection 2.1.1 and subsection 3.2.

This may imply a different evolutionary future of the host galaxy of each radio source. For example, the PKS 1138−262 host may evolve into the centrally-dominant cD-like galaxy relatively early, while the 4C 23.56 host may remain one of several dominant galaxies until they merge into a single larger galaxy at the center of the potential. The host of 4C 23.56 is indeed ~ 1.5 magnitudes less luminous in $K_{\rm s}$ than the PKS 1138 host ($K_{\rm s} = 18.66$ after removing nuclear component and emission-line contribution; Pentericci et al. 1997). Furthermore, the $K_{\rm s} = 18.66$ magnitude for the host of PKS 1138 is unusual; its apparent magnitude is as bright as the brightest cluster galaxies at $z = 1.5$ (Collins et al. 2009). If we use formula (6) in sub-subsection 3.5.3, the stellar mass of the 4C 23.56 and the PKS 1138 hosts are estimated to be $4.7 \times 10^{11}\,M_{\odot}$ and $5.5 \times 10^{12}\,M_{\odot}$, respectively. For a comparison, Seymour et al. (2007) estimated the stellar mass of both host galaxies based on their Spitzer multi-band photometry, finding $3.9 \times 10^{11}\,M_{\odot}$ and $< 1.3 \times 10^{12}\,M_{\odot}$, for 4C 23.56 and PKS 1138 respectively.

Another difference is in the number of HAEs with strong ($EW_{\rm o} > 100$ Å) emission. In the 4C 23.56 field, 10 of 11 HAEs have rest-frame $EW_{\rm o} > 100$ Å. In the PKS 1138 field the number of objects that satisfy $EW_{\rm o} > 100$ Å and $NB_{\rm Vega} < 20.2$ is 5. Since the equivalent width relates to the Hα luminosity, the excess number of strong *EW* objects in the 4C 23.56 field implies more active star formation occurring in that protocluster. We address this quite interesting topic more in the next section.

Recently, Hayashi et al. (2010) reported an excess of [O II] emitters in the field of the distant X-ray cluster XMMXCS J2215.9−1738 at $z = 1.46$. The distribution of [O II] emitters are prevalent from the outskirt to the core region of the X-ray cluster. They showed that the fraction of [O II] emitters among all cluster members as well as the level of the star-formation are shown to be both nearly constant as a function of clustercentric radius (see also, Tran et al. 2010).

Their figures 5–7 indicate that the distribution of the emitters well traces the overall distribution of all cluster members. The distribution of Hα emitters in Kurk et al. (2004a) also closely matches the photo-*z*-selected galaxy distribution, as shown by their figure 6 (Tanaka et al. 2010). We note, however, that the case of the cluster XMMXCS J2215.9−1738 may not be as representative as a cluster at $z \sim 1.5$. Hilton et al. (2010) has shown that the system has a possible bimodal kinematic structure, with the position of the cluster BCG being significantly offseted from the center of the thermal hot X-ray gas. Also, the NB HAE survey for another cluster XMMU J2235.3−2557 at $z \sim 1.4$ by Bauer et al. (2011) has shown that the HAE distribution just avoids the central ~ 200 kpc of the cluster core (see also Lidman et al. 2008; Strazzullo et al. 2010). Although we are still not sure about whether the HAE can trace the overall distribution of cluster galaxies from the core to the outskirts at $z > 2$ universe, both studies could consider the supporting case that the distribution of HAEs in the 4C 23.56 protocluster also traces the underlying galaxy distribution. Future analysis based on the broadband imaging will enable us to address this issue.

Hayashi et al. (2010) contrasted the activity of galaxies in the cluster core region by comparing to similar work for a $z = 0.8$ cluster by Koyama et al. (2010). At even lower redshift, Kodama et al. (2004) studied the HAE distribution for Cl 0024+1652 at $z = 0.4$, showing a quite strong suppression of activity in the cluster core region. It is quite interesting to connect the results by these works from $z = 0.4$ (Kodama et al. 2004), $z = 0.8$ (Koyama et al. 2010), $z = 1.4$–1.5 (Hayashi et al. 2010; Bauer et al. 2011), $z = 2.1$–2.2 (Kurk et al. 2004a; Gobat et al. 2011), to our $z = 2.5$ studies as a snapshot of the cluster evolution in each epoch (Tadaki et al. 2011). The implied rise of star-formation activity in the cluster core with the redshift and its variety suggests that, while it may indicate that we are gradually approaching the era of galaxy formation for members in the cluster core (Kodama & Bower 2001), it is important to evaluate the physical state (richness, dynamics, mass, etc.) for each protoclusters in detail to draw a general pictures of early history of galaxy evolution in the cluster core. Detailed studies of larger samples are clearly needed to corroborate this apparent evolutionary trend.

4.3. Star-Formation Activity of HAEs

In subsection 3.5 we calculate the *SFR* and the stellar mass of our HAE sample. Although we admit that the estimate of these values is rather crude, here we try to characterize the star formation of the HAEs in the 4C 23.56 field by comparing them to other studies. As discussed in subsection 3.5, the main uncertainty for Hα-based *SFR* is in the estimate of the dust extinction, as indicated by MIPS detection. The unknown fraction of the AGN contribution to our HAE sample (it can be non-negligible: see Lehmer et al. 2009; Digby-North et al. 2010; Lemaux et al. 2010) is also an issue that we need to address by future observations.

In figure 11a, we plot the estimated star-formation rate of our HAEs against their stellar mass. The minimum *SFR* in our sample is $\sim 15\,M_{\odot}\,{\rm yr}^{-1}$, with a median value of 45 (182 for extinction corrected, 746 for MIPS) $M_{\odot}\,{\rm yr}^{-1}$. In the figure, the brightest object with the highest *SFR*, is 4C 23.56 (note that the mass estimate for this object is probably overestimated, not only due to the inclusion of AGN but also due to the effect of the poor sky subtraction: see subsection 2.1). The line on the figure is the average mass–*SFR* relation for $z \sim 2$ BzK-selected galaxies with MIPS detections by Daddi et al. (2007). The *SFR*s based on both indicators show larger values than expected from the $z \sim 2$ mass–*SFR* relation by Daddi et al. (2007). Especially, the MIPS-based *SFR* shows large excess. This trend seems to be real, because our MIPS-based *SFR* is derived from the same equation as used by Daddi et al. (2007). This may indicate that some galaxies in the protocluster 4C 23.56 have higher star-formation activity than the field counterparts with similar mass.

The observed large excess of the 24 μm-based *SFR* relative to Hα-based one may indicate that the star-formation activity in our HAE sample is largely (or selectively) hidden by dust. At lower redshifts such hidden star-formation activity revealed by infrared observation is often reported (e.g., Valdés et al. 2005; Geach et al. 2006; García-Marín et al. 2009; Garn et al. 2010). On the other hand, the recent calibration of the MIPS 24 μm-based *SFR* for star-forming galaxies at $z \sim 2$ by the Herschel PACS observation has revealed that the *SFR*s from 24 μm alone could be overestimated by a factor of ~ 2–7.5

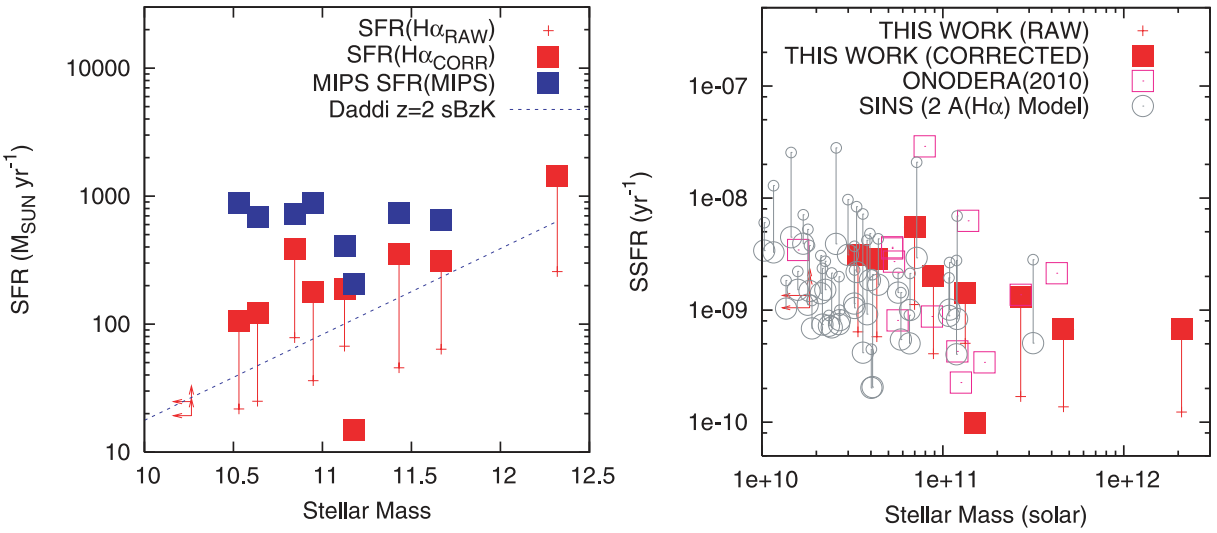

Fig. 11. (a: left) Observed star-formation rate (*SFR*) of the HAE sample as a function of stellar mass. The plus marks indicate the Hα-based *SFR* before the extinction correction, while red filled box connected to each plus mark is its extinction-corrected *SFR* values (see text). The blue filled boxes are the *SFR* based on the Spitzer MIPS 24 μm photometry. The dotted line (blue) indicates the mass–*SFR* relation at $z \sim 2$ from Daddi et al. (2007). The two arrows indicate the objects with the upper-(lower-) limit for their mass (*SFR* before extinction correction) due to their faintness. The most massive object is 4C 23.56. Its MIPS-based *SFR* is not shown (due to an AGN contribution and the model limit). (b: right) The comparison of the Hα-based specific *SFR* (*SSFR*) of our HAE sample and of some field Hα-emitting objects as a function of stellar mass. The marks with dust extinction correction (red filled box) and raw values (plus) are connected by vertical lines. The field samples are from Förster-Schreiber et al. (2009) and Onodera et al. (2010). Note that Förster-Schreiber et al. (2009) shows the results using two types of the extinction correction; thus, they are shown as connected vertical lines in the figure. Our *SSFR* estimate should be treated as crude values due to the large uncertainty in both the extinction correction and the mass estimate. Note that 4C 23.56 is the point at $M > 10^{12}\,M_{\odot}$, and should be ignored because of strong AGN contamination in both the K-band and the Hα emission.

(Nordon et al. 2010; Rodighiero et al. 2010). Our observed trend can be due to the large systematics in the estimate of the total infrared luminosity from the rest-frame 8 μm photometry. For now we do not know whether the HAEs in the 4C 23.56 field harbours the star formation significantly hidden by dust. A direct far-infrared observation by ALMA will address the issue.

In figure 11b we show the L(Hα)-based specific star-formation rate (*SSFR*) as a function of the stellar mass. For a comparison, we plot the *SSFR* values for field Hα emitters from Förster-Schreiber et al. (2009) and Onodera et al. (2010). The Förster-Schreiber et al. (2009) points include two types of the extinction correction, which are shown as connected points with vertical lines in the figure, while Onodera et al. (2010) used a correction (described above) that could be considered to be the middle between the two extreme cases from Förster-Schreiber et al. (2009).

The measured relation between *SSFR* and mass clearly deviates from that observed in similar studies of low-redshift clusters. For example, Patel et al. (2009) measured the *SFR* and *SSFR* of a rich cluster at $z \sim 0.8$ from MIPS-based photometry, and confirmed that the *SSFR* of massive ($\log M/M_{\odot} > 10.8$) galaxies in high density regions is as low as that for field objects with similar mass in the local universe. Also, at $z > 1$, the *SSFR* estimate of the member galaxies in the irregular cluster CL 0332−2742 at $z \sim 1.6$ by Kurk et al. (2009) show that significant member galaxies have much lower *SSFR* values than field counterparts at similar redshifts, despite that the system is quite irregular and far from a virialized structure. Recently, Tanaka et al. (2010) studied galaxies in the protocluster around PKS 1138 at $z = 2.16$ and showed a similar trend of the suppressed star-formation activity in the cluster compared to the field environment (see also, Zirm et al. 2008). These studies may indicate that the star-formation activity in cluster environment is suppressed by up to $z \sim 2$.

To avoid uncertainties introduced by estimating the *SFR* and the stellar mass, we also compared the star-formation rates directly using the observed values. In figure 12 we show the observed K-band magnitude versus the Hα luminosity [L(Hα)] of the same dataset, as shown in figure 11b, but limited to objects at $z > 2$. Here, the data from Kurk et al. (2004a) are also added for a comparison. Within the uncertainties, all HAEs in the 4C 23.56 field are clearly as luminous as the brightest Hα sample in the general field results, again suggesting an excess of active star formation in the 4C 23.56 field.

Perhaps more interestingly, in figure 12 we compare the HAEs in the 4C 23.56 field with the PKS 1138 field data. The majority of HAEs in the PKS 1138 protocluster have lower Hα luminosities than both field objects, and the HAEs in 4C 23.56 despite being within a similar K magnitude range. This indicates that the HAEs in the PKS 1138 field show suppressed star formation. This is actually the same conclusion as that reached by Tanaka et al. (2010), but their work was based on broadband SED fitting, i.e., from an independent measure.

The cosmic time between the two protoclusters is only 0.4 Gyr. This is actually long enough to discern changes in the star-formation activity if their star-formation timescale is short. Tanaka et al. (2010) suggested that the star-formation timescale for galaxies in the PKS 1138 field is much shorter than that

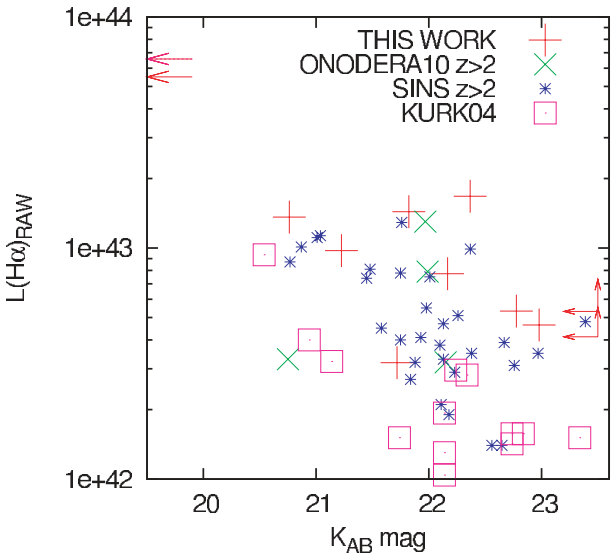

Fig. 12. Comparison of the K_s magnitude and $L(\mathrm{H}\alpha)$ for Hα emitters from two field surveys from Förster-Schreiber et al. (2009) and Onodera et al. (2010) (asterisk and cross), PKS 1138−262 field from Kurk et al. (2004a) (box), and our study (plus). Only objects at $z > 2$ are shown for field survey data. For the PKS 1138 field, we plot the data with a significance level over 3 and $EW_o > 50$ Å for a better match to our selection criteria. Two arrows at brighter than $K = 20$ represents the PKS 1138 and 4C 23.56 radio galaxies which are out of the figure due to their bright magnitudes.

for galaxies with similar mass in the GOODS fields. Their figure 13 demonstrates a rapid decline of the *SFR* in the protocluster compared to that of GOODS, and shows that the time difference of 0.4 Gyr is long enough to observe the decline. For example, if we suppose that these star-forming galaxies in protoclusters are formed at $z \sim 3$, the increase in the star-formation rate between $z = 2.16$ to 2.5 (0.4 Gyr) is close to an order of magnitude.

This argument could of course be too simplified, because it assumes that any galaxies in the two clusters have almost the same formation period around $z \sim 3$. The actual formation of massive galaxies in the cluster environment could be much more complicated, and it could be coupled with the fundamental cluster properties (mass, merger history, dynamical state, and so on). As already discussed, the difference of the star-formation activity between the two protoclusters might be related to the different inherent cluster characteristics. The PKS 1138 host is exceptionally massive, and already lies near the apparent center of the galaxy distribution (Kurk et al. 2004a; Seymour et al. 2007), while the 4C 23.56 host lies at the edge of the HAE (and presumably overall galaxy) distribution (subsections 3.2 and 4.2). The soft X-ray emission from the hot intracluster gas is (marginally) detected in PKS 1138 (Carilli et al. 2002), while for 4C 23.56 it is not (Johnson et al. 2007). The future of the PKS 1138 protocluster may well be an X-ray bright, well-evolved rich cluster with a massive cD galaxy lying in the center, while that of 4C 23.56 might be an X-ray faint cluster with a few dominant giant ellipticals near the center of the potential, such as the Coma or Virgo clusters.

5. Summary

We have discovered a significant excess of near-infrared selected emission-line objects around the radio galaxy 4C 23.56 at $z = 2.486$. We detected 11 robust emission-line galaxies with a line flux greater than 7.5×10^{-17} erg s^{-1} cm^{-2} in our MOIRCS imaging observation of the $4' \times 7'$ field around the radio galaxy. We show that this is a significantly higher (5 times more) detection rate compared to other near-infrared emission-line surveys in non–radio-galaxy fields. Three of the emission-line galaxies are found to have a spectroscopic redshift of $z = 2.49$. We therefore conclude there is a protocluster physically associated with 4C 23.56.

The distribution of HAEs on the sky is confined to a relatively small area (~ 1.2 Mpc-radius region) near the radio galaxy, with 4C 23.56 placed at the western edge. We show that this is not due to an observational bias, and conclude that the protocluster is physically associated with the radio galaxy. The offset position of the radio galaxy is interesting, because the hosts of powerful radio galaxies are usually very massive and often assumed to be the dominant object (e.g., cD galaxy) in the center of the cluster. We also find that there is an interesting compact group of four HAEs, all the members of which show offset Hα emission relative to the K_s-band light position. This may indicate strong star formation on the edge of each galaxy, which is occurring due to strong interactions with the group. A more exotic interpretation might be that there is ram-pressure stripping of the galactic-scale Hα-emitting gas by the hot intracluster gas. Further follow-up is necessary to understand this phenomenon.

Our analysis of deep Spitzer MIPS 24 μm data for 4C 23.56 shows that all but two of the HAEs have 24 μm counterparts. The inferred star-formation rate (*SFR*) based on MIPS 24 μm photometry is quite high (median of $> 700\,M_\odot\,\mathrm{yr}^{-1}$), indicating that intense starburst activity is occurring in each HAE. The MIPS-based *SFR* is on average 3.5 times higher than the value inferred from the observed Hα luminosity. The strong effect of "selective" dust extinction is evident for these galaxies, implying metal-rich and evolved populations for HAEs, as suggested by Kurk et al. (2004a).

An analysis of the spatial distribution of the MIPS sources has also revealed that there exists a strong excess around 4C 23.56. Notably, the distribution of sources that have 24 μm fluxes as faint as the HAEs (90–275 μJy) shows the same offset distribution relative to the radio galaxy, and the position of the density peak nicely coincides with the HAE distribution. This is another indication that strong star-formation activity is going on in the protocluster.

A comparison of the star-formation rates of HAEs in the protocluster 4C 23.56 at $z = 2.48$ to those in another protocluster PKS 1138−262 at $z = 2.16$ and to those in the general field at $z \sim 2$ shows that: (1) HAEs in the 4C 23.56 field are as active as those in the general field, and that (2) HAEs in the protocluster PKS 1138−262 show a clear *deficit* of objects with high Hα luminosities. The clear difference in star-forming activities between the two protoclusters at similar redshifts may indicate that we are stepping into an epoch of major star formation in massive cluster galaxies. Given the fact that there is a small, but significant, time difference of 0.4 Gyr between

the two redshifts, such variation in star-formation activity may be interpreted as a time evolution where star-formation activities to form massive galaxies can decay rather sharply during this epoch ($2 < z < 3$) in proto-clusters (e.g., Kodama et al. 2007; Tanaka et al. 2010). Alternatively, we may be just seeing the intrinsic scatter of cluster properties at this high redshift where the onset of cluster formation and the subsequent evolution depend on the mass of the systems and/or structures in the surrounding environment. Such a dependence is actually inferred in lower-redshift clusters at $z < 1$ (e.g., Urquhart et al. 2010). However, we do not yet know the global properties of these protoclusters, such as the total number of member galaxies, cluster masses, and the dynamical states, nor do we yet have a statistical sample of protoclusters at this interesting redshift regime to disentangle these two effects. We are desperate to obtain such information by extensive near-infrared spectroscopy and to increase the sample of proto-clusters at $z > 2$.

We thank an anonymous referee for comments that lead to improvements of the paper. We thank the MOIRCS Deep Survey Team for providing us with the MODS catalog. Also, we would like to thank Dr. Sune Toft and Dr. Masa Tanaka, and many others for useful comments and suggestions. We also thank Dr. Ryuji Suzuki for providing simulation data on the shift of the central wavelength of *NB* filters. This work was supported by the JSPS Institutional Program for Young Researcher Overseas Visits. This work was also partly supported by the Visitor Programs by the ESO. YT and TK thank for support via Grant-in-Aid for Scientific Research (KAKENHI: Nos. 19340046 and 21340045, respectively) by the Ministry of Education, Culture, Sports, Science and Technology in Japan. JK thanks the DFG for support via German-Israeli Project Cooperation grant STE1869/1-1.GE625/15-1. IT would like to thank the all ESO staff for the hospitality during the stay in ESO Garching. IT would also like to thank all staffs and members of the DARK Cosmology Center, MSSL University College London, and Durham University for their warm hospitality during my stay related to this study. This work is based on data collected at Subaru Telescope, which is operated by the National Astronomical Observatory of Japan. This is also based in part on observations made with the Spitzer Space Telescope, which is operated by the Jet Propulsion Laboratory, California Institute of Technology under a contract with NASA, as well as the data collected by the 4.2 m William Herschel Telescope which is operated on the island of La Palma by the Isaac Newton Group in the Spanish Observatorio del Roque de los Muchachos of the Instituto de Astrofísica de Canarias.

Appendix 1. The *BJK* Color Selection for Rejecting Objects at $z < 1$

In order to reject the possibility that our single-line detection by *NB* filter, or that the spectra is mainly from the low-redshift Paschen series interlopers, we introduce broadband color selection by the $B - J$ versus $J - K_s$ two-color diagram. Here, we show its effectiveness using the large photometric/spectroscopic catalog for the GOODS-North region.

We make use of the MOIRCS Deep Survey Catalog, which contains 13-band photometric data as well as an extensive compilation of spectroscopic redshift data (Kajisawa et al. 2011). In figure 5a, we plot the color of all galaxies with $K_s < 23$ in GOODS-N (gray crosses). The galaxies at $0.2 < z < 0.25$ and $0.75 < z < 0.8$ (spectroscopically measured), each of which includes the Paα and Paβ interlopers, are shown by blue filled triangles, while the objects at $2.3 < z < 2.6$, which include the 4C 23.56 redshift, are shown by red filled circles. There is a clear line between the two samples. Here we define it as

$$(J - K_s) = 0.4\,(B - J) - 0.2, \tag{A1}$$

which is shown as the magenta dotted line in the figure. The insetted diagram in figure 5b shows the fraction of galaxies whose $J - K_s$ color is redder than the line defied here ("*BJK*" galaxies) as a function of redshifts (spectroscopic redshift sample only). Almost no objects at $z < 1.2$ can be *BJK* galaxies, while more than 80% of objects at $z \sim 2.5$ satisfy the criterion.

We also calculated the behavior of galaxy colors in the *BJK* plane using the population synthesis SED models by Kodama and Arimoto (1997) overplotted in figure 5a. In the figure, each model track indicates, from bluer to redder, the "pure disk" model with continuous *SFR* (bluest), "50% disk + 50% bulge", "20% disk + 80% bulge", and "pure bulge" model with the formation redshift of 5 (reddest, and mostly out of the figure). In each model, symbols are put from $z = 0.1$ to 4, with an interval of 0.5 from $z = 0.5$ (each line starts from $z = 0.1$ with a symbol, and ends at 4.5 without symbol). A part of each model track has a region with cyan-colored solid line, which indicates the region at $2 < z < 3.8$. The extinction vector for $A_V = 1.0$ based on Calzetti (2001) is also plotted.

The behavior of the model tracks also confirms that the our proposed dividing line for *BJK* galaxies works rejecting objects at $z < 1$. The model tracks at $2.3 < z < 2.6$ (the same redshift range as red filled circles in figure 5b) tend to go a bit further from the *BJK* line than the actual distribution of objects at the same redshift range in figure 5b. This may be explained, though, by a difference in the metallicity between the modeled and observed galaxies. More advanced modeling is beyond the scope of this paper, however.

Appendix 2. Objects Identified in Previous Studies

As is described in section 1, the 4C 23.56 field was also observed previously by KC97, Kajisawa et al. (2006b), and Stockton et al. (2004). Here we briefly comments on the objects detected in each study.

Objects in KC97

KC97 studied the 1.25 arcmin^2 region around the radio galaxy using deep $U'VIK$ imaging data from 2.2- and 3.6-m telescopes. They also searched for Lyα emitters using the narrowband filter at 4229 Å on the UH 2.2-m telescope. They cataloged 9 possible Lyα-emitting companions and 15 EROs selected by $I - K_s$ colors around the radio galaxy.

We first looked for counterparts of their Lyα emitters in our K_s image. However, we could only identify one object (ID #110 in their catalog). Since the $K_s - NB$ color of the object

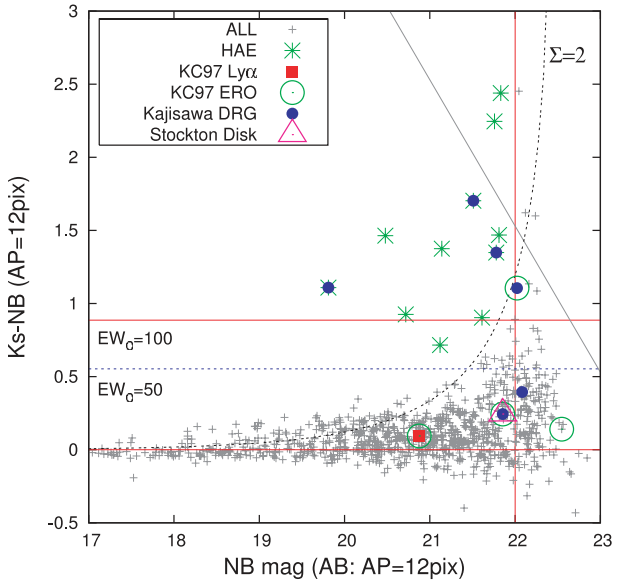

Fig. 13. Color excess of objects studied by others in the 4C 23.56 field. Only objects identified in our catalog are shown here. The gray plus marks are all objects in the field of view, and the asterisks are the HAEs. A red filled box and 4 green open circles each indicate a Ly α emitter and the EROs from KC97 that are in our catalog. Blue-filled circles indicate the DRG sample from Kajisawa et al. (2006b), and a magenta open triangle is the object studied by Stockton et al. (2004). Ignoring the radio galaxy, three DRGs/EROs show the emission-line excess ($K_s - NB > 1$), and they are also plotted in figure 6.

is 0.14, no clear sign of *NB* excess can be seen in figure 13 (red filled box).

Next we identify their EROs. Of their 15 objects, 6 objects are not seen at all in our K_s nor *NB* images, and 5 objects are quite faint and subsequently not in our SExtrctor catalog. Note that their data is extremely deep, with a 3σ limiting magnitude of $K = 24.3$ mag, while our data only reach 23.5 mag. Among the 4 remaining objects, only one object (their ID #70) shows a sign of emission-line excess (green open circles in figure 13). However, the object is just below our HAE selection criteria ($NB < 22$ mag and $\Sigma > 2$), and therefore not present among our HAE candidates.

We comment on the failure of the HAE counterpart detection for their Ly α emitters in detail. We can calculate the expected Hα flux from their cataloged equivalent width, assuming the Ly α/Hα ratio of 8.7 for the Case B recombination (Osterbrock 1989). We find that the expected Hα flux are mostly several times 10^{-17} erg s^{-1} cm^{-2}, close to our detection limit. However, this should be considered as a lower limit, since the Ly α/Hα can be much smaller than 8.7 due to more effective dust absorption by the resonant scattering nature of the Ly α line (Kurk et al. 2004a; Hayes et al. 2010b). Thus, at least some, if not all, of their 9 LAEs could be detected. We note that the cataloged K-band magnitudes of Ly α emitters are all quite faint (5 are upper limits with $K_{AB} > 24.35$, and only two are within our magnitude limit of $K_{AB} > 23.5$). The non-detection by our K image could be reasonable. However, they are also totally absent, even in our *NB2288* image.

Kurk et al. (2004a) also did not detect Hα emission for their sample of Ly α emitters in the PKS 1138 protocluster. For two of their three brightest Ly α emitters, for which Hα emission could be detectable, faint emission was seen, but not strong enough to pass the HAE selection criteria. The range of the upper limit of the Lyα/Hα ratio for their Hα emitters are 0.03–1.06, significantly lower than the Case-B assumption (see also, Hayes et al. 2010b).

There are two possibilities to explain this. One is that the redshift of the Ly α emitters is out of our *NB2288* narrowband window. The filter used by KC97 has a central wavelength of 4229 Å with a filter width of 70 Å. The Ly α emission that can enter into the window should be in the range $2.45 < z < 2.50$, and the corresponding Hα line will come to 2.261–2.294 μm. As is shown in figure 1, almost half of the shorter wavelength range (2.261–2.28 μm) is out of our survey window. However, if the Ly α emitters are all such objects, they would not be associated with, but slightly foreground to 4C 23.56.

Another explanation is a large error in the Ly α *EW* estimate, or spurious detections. Due to a lack of B-band data which samples the continuum just redwards of Ly α, they had to use a crude UV continuum estimate. If the *EW* of their Ly α emitters are much smaller than their quoted values, our non-detection of Hα counterparts could be understood. An independent Ly α emitter search is necessary to check the reliability of their selection of *NB* excess objects. We are in the progress of carrying out such a Ly α imaging survey for this field. Its results will be published elsewhere (I. Tanaka et al., in preparation).

Objects in Kajisawa et al. (2006b)

Kajisawa et al. (2006b) took the *JHK* images of the 4C 23.56 field and found a significant excess of "*JHK*" objects (see also, Kodama et al. 2007). We checked their Hα excess in our catalog. Though we could not identify their b-*JHK* objects, several Distant Red Galaxies (DRGs) were identified. The color excess of their DRGs is shown in figure 13 (blue filled circles). Excluding 4C 23.56, two objects are identified in our HAE sample. Another two objects are identified as KC97's EROs. One of them shows emission-line excess (#70 in KC97). Two other objects do not show detectable emission-line excess.

An Object in Stockton et al. (2004)

Stockton et al. (2004) reported an object in 4C 23.56 having very red color and a disk-like morphology. The SED fitting result indicates a strong preference for the single-burst model with fairly old age of $\sim$2 Gyr at the redshift of the radio galaxy. The result suggests that the galaxy should be inactive Stockton and McGrath (2007), and no Hα emission is expected.

Their object is actually identified as an ERO in KC97, which is a DRG in Kajisawa et al. (2006b). In figure 13 we show the color excess of the object (magenta open triangle). As expected, the object does not show signs of excess emission from Hα.

References

Afonso, J., Hopkins, A., Mobasher, B., & Almeida, C. 2003, ApJ, 597, 269
Balogh, M. L., Morris, S. L., Yee, H. K. C., Carlberg, R. G., & Ellingson, E. 1997, ApJ, 488, L75
Bauer, A. E., Grützbauch, R., Jørgensen, I., Varela, J., & Bergmann, M. 2011, MNRAS, 411, 2009
Bertin, E., & Arnouts, S. 1996, A&AS, 117, 393
Blanton, M. R., & Moustakas, J. 2009, ARA&A, 47, 159
Bower, R. G., Kodama, T., & Terlevich, A. 1998, MNRAS, 299, 1193
Bower, R. G., Lucey, J. R., & Ellis, R. S. 1992, MNRAS, 254, 601
Bruzual, G., & Charlot, S. 2003, MNRAS, 344, 1000
Bundy, K., et al. 2006, ApJ, 651, 120
Butcher, H., & Oemler, A., Jr. 1978, ApJ, 219, 18
Butcher, H., & Oemler, A., Jr. 1984, ApJ, 285, 426
Calzetti, D. 2001, PASP, 113, 1449
Carilli, C. L., Harris, D. E., Pentericci, L., Röttgering, H. J. A., Miley, G. K., Kurk, J. D., & van Breugel, W. 2002, ApJ, 567, 781
Chabrier, G. 2003, PASP, 115, 763
Chary, R., et al. 2004, ApJS, 154, 80
Chary, R., & Elbaz, D. 2001, ApJ, 556, 562
Cid Fernandes, R., Mateus, A., Sodré, L., Jr., Stasińska, G., & Gomes, J. M. 2005, MNRAS, 358, 363
Clemens, M. S., Bressan, A., Nikolic, B., Alexander, P., Annibali, F., & Rampazzo, R. 2006, MNRAS, 370, 702
Clemens, M. S., Bressan, A., Nikolic, B., & Rampazzo, R. 2009, MNRAS, 392, L35
Collins, C. A., et al. 2009, Nature, 458, 603
Cortese, L., et al. 2007, MNRAS, 376, 157
Cortese, L., Gavazzi, G., Boselli, A., Franzetti, P., Kennicutt, R. C., O'Neil, K., & Sakai, S. 2006, A&A, 453, 847
Couch, W. J., Ellis, R. S., Sharples, R. M., & Smail, I. 1994, ApJ, 430, 121
Daddi, E., et al. 2007, ApJ, 670, 156
Daddi, E., Cimatti, A., Renzini, A., Fontana, A., Mignoli, M., Pozzetti, L., Tozzi, P., & Zamorani, G. 2004, ApJ, 617, 746
Dale, D. A., & Helou, G. 2002, ApJ, 576, 159
De Breuck, C., et al. 2004, A&A, 424, 1
De Breuck, C., van Breugel, W., Stanford, S. A., Röttgering, H., Miley, G., & Stern, D. 2002, AJ, 123, 637
De Lucia, G., et al. 2004, ApJ, 610, L77
De Lucia, G., et al. 2007, MNRAS, 374, 809
Digby-North, J. A., et al. 2010, MNRAS, 407, 846
Dijkstra, M., & Loeb, A. 2009, MNRAS, 400, 1109
Doherty, M., et al. 2010, A&A, 509, A83
Dressler, A. 1980, ApJ, 236, 351
Dressler, A., et al. 1997, ApJ, 490, 577
Dressler, A., Oemler, A., Jr., Butcher, H. R., & Gunn, J. E. 1994, ApJ, 430, 107
Eke, V. R., Navarro, J. F., & Frenk, C. S. 1998, ApJ, 503, 569
Elbaz, D., et al. 2007, A&A, 468, 33
Elbaz, D., Cesarsky, C. J., Chanial, P., Aussel, H., Franceschini, A., Fadda, D., & Chary, R. R. 2002, A&A, 384, 848
Ellingson, E., Lin, H., Yee, H. K. C., & Carlberg, R. G. 2001, ApJ, 547, 609
Ellis, S. C., Jones, L. R., Donovan, D., Ebeling, H., & Khosroshahi, H. G. 2006, MNRAS, 368, 769
Ellis, R. S., Smail, I., Dressler, A., Couch, W. J., Oemler, A., Jr., Butcher, H., & Sharples, R. M. 1997, ApJ, 483, 582
Erb, D. K., Steidel, C. C., Shapley, A. E., Pettini, M., Reddy, N. A., & Adelberger, K. L. 2006, ApJ, 647, 128
Förster Schreiber, N. M., et al. 2009, ApJ, 706, 1364
Franx, M., et al. 2003, ApJ, 587, L79
García-Marín, M., Colina, L., & Arribas, S. 2009, A&A, 505, 1017
Garn, T., et al. 2010, MNRAS, 402, 2017
Geach, J. E., et al. 2006, ApJ, 649, 661
Geach, J. E., et al. 2010, MNRAS, 402, 1330
Geach, J. E., Smail, I., Best, P. N., Kurk, J., Casali, M., Ivison, R. J., & Coppin, K. 2008, MNRAS, 388, 1473
Gehrels, N. 1986, ApJ, 303, 336
Gilbank, D. G., Yee, H. K. C., Ellingson, E., Gladders, M. D., Loh, Y.-S., Barrientos, L. F., & Barkhouse, W. A. 2008, ApJ, 673, 742
Gobat, R., et al. 2011, A&A, 526, A133
Gómez, P. L., et al. 2003, ApJ, 584, 210
Hashimoto, Y., Oemler, A., Jr., Lin, H., & Tucker, D. L. 1998, ApJ, 499, 589
Hayashi, M., Kodama, T., Koyama, Y., Tanaka, I., Shimasaku, K., & Okamura, S. 2010, MNRAS, 402, 1980
Hayes, M., et al. 2010b, Nature, 464, 562
Hayes, M., Schaerer, D., & Östlin, G. 2010a, A&A, 509, L5
Hilton, M., et al. 2009, ApJ, 697, 436
Hilton, M., et al. 2010, ApJ, 718, 133
Holden, B. P., Stanford, S. A., Eisenhardt, P., & Dickinson, M. 2004, AJ, 127, 2484
Hopkins, A. M., Connolly, A. J., Haarsma, D. B., & Cram, L. E. 2001, AJ, 122, 288
Ichikawa, T., et al. 2006, Proc. SPIE, 6269,
Ideue, Y., et al. 2009, ApJ, 700, 971
Johnson, O., Almaini, O., Best, P. N., & Dunlop, J. 2007, MNRAS, 376, 151
Kajisawa, M., et al. 2000, PASJ, 52, 61
Kajisawa, M., et al. 2006b, PASJ, 58, 951
Kajisawa, M., et al. 2009, ApJ, 702, 1393
Kajisawa, M., et al. 2011, PASJ, 63, S379
Kajisawa, M., Kodama, T., Tanaka, I., Yamada, T., & Bower, R. 2006a, MNRAS, 371, 577
Keel, W. C., Cohen, S. H., Windhorst, R. A., & Waddington, I. 1999, AJ, 118, 2547
Kennicutt, R. C., Jr. 1998, ARA&A, 36, 189
Knopp, G. P., & Chambers, K. C. 1997, ApJS, 109, 367 (KC97)
Kodama, T., et al. 2004, MNRAS, 350, 1005
Kodama, T., & Arimoto, N. 1997, A&A, 320, 41
Kodama, T., Arimoto, N., Barger, A. J., & Arag′on-Salamanca, A. 1998, A&A, 334, 99
Kodama, T., & Bower, R. G. 2001, MNRAS, 321, 18
Kodama, T., Tanaka, I., Kajisawa, M., Kurk, J., Venemans, B., De Breuck, C., Vernet, J., & Lidman, C. 2007, MNRAS, 377, 1717
Koyama, Y., Kodama, T., Shimasaku, K., Hayashi, M., Okamura, S., Tanaka, I., & Tokoku, C. 2010, MNRAS, 403, 1611
Kurk, J. D., et al. 2000, A&A, 358, L1
Kurk, J., et al. 2009, A&A, 504, 331
Kurk, J. D., Pentericci, L., Overzier, R. A., Röttgering, H. J. A., & Miley, G. K. 2004b, A&A, 428, 817
Kurk, J. D., Pentericci, L., Röttgering, H. J. A., & Miley, G. K. 2004a, A&A, 428, 793
Leggett, S. K., et al. 2006, MNRAS, 373, 781
Lehmer, B. D., et al. 2009, ApJ, 691, 687
Lemaux, B. C., Lubin, L. M., Shapley, A., Kocevski, D., Gal, R. R., & Squires, G. K. 2010, ApJ, 716, 970
Lidman, C., et al. 2008, A&A, 489, 981

Magorrian, J., et al. 1998, AJ, 115, 2285
Matsuda, Y., et al. 2004, AJ, 128, 569
Matsuda, Y., et al. 2009, MNRAS, 400, L66
Mei, S., et al. 2009, ApJ, 690, 42
Moorwood, A. F. M., van der Werf, P. P., Cuby, J. G., & Oliva, E. 2000, A&A, 362, 9
Nakata, F., Bower, R. G., Balogh, M. L., & Wilman, D. J. 2005, MNRAS, 357, 679
Nordon, R., et al. 2010, A&A, 518, L24
Oemler, A., Jr., Dressler, A., & Butcher, H. R. 1997, ApJ, 474, 561
Onodera, M., Arimoto, N., Daddi, E., Renzini, A., Kong, X., Cimatti, A., Broadhurst, T., & Alexander, D. M. 2010, ApJ, 715, 385
Osterbrock, D. E. 1989, Astrophysics of gaseous nebulae and active galactic nuclei (Mill Valley, CA: University Science Books), 422
Packham, C., et al. 2003, MNRAS, 345, 395
Pannella, M., et al. 2009, ApJ, 701, 787
Papovich, C., et al. 2007, ApJ, 668, 45
Papovich, C., et al. 2010, ApJ, 716, 1503
Patel, S. G., Holden, B. P., Kelson, D. D., Illingworth, G. D., & Franx, M. 2009, ApJ, 705, L67
Pentericci, L., et al. 2000, A&A, 361, L25
Pentericci, L., Roettgering, H. J. A., Miley, G. K., Carilli, C. L., & McCarthy, P. 1997, A&A, 326, 580
Poggianti, B. M., et al. 2006, ApJ, 642, 188
Poggianti, B. M., et al. 2008, ApJ, 684, 888
Poggianti, B. M., Bridges, T. J., Komiyama, Y., Yagi, M., Carter, D., Mobasher, B., Okamura, S., & Kashikawa, N. 2004, ApJ, 601, 197
Poggianti, B. M., Smail, I., Dressler, A., Couch, W. J., Barger, A. J., Butcher, H., Ellis, R. S., & Oemler, A., Jr. 1999, ApJ, 518, 576
Rakos, K., Schombert, J., & Odell, A. 2008, ApJ, 677, 1019
Rees, M. J. 1985, MNRAS, 213, 75
Rieke, G. H., Alonso-Herrero, A., Weiner, B. J., Pérez-González, P. G., Blaylock, M., Donley, J. L., & Marcillac, D. 2009, ApJ, 692, 556
Rodighiero. G., et al. 2010, A&A, 518, L25
Röttgering, H. J. A., van Ojik, R., Miley, G. K., Chambers, K. C., van Breugel, W. J. M., & de Koff, S. 1997, A&A, 326, 505
Salpeter, E. E. 1955, ApJ, 121, 161
Savaglio, S., et al. 2005, ApJ, 635, 260
Seymour, N., et al. 2007, ApJS, 171, 353
Shimasaku, K., et al. 2003, ApJ, 586, L111
Sobral, D., Best, P. N., Smail, I., Geach, J. E., Cirasuolo, M., Garn, T., & Dalton, G. B. 2011, MNRAS, 411, 675
Stanford, S. A., Eisenhardt, P. R., & Dickinson, M. 1998, ApJ, 492, 461
Steidel, C. C., Adelberger, K. L., Dickinson, M., Giavalisco, M., Pettini, M., & Kellogg, M. 1998, ApJ, 492, 428
Steidel, C. C., Adelberger, K. L., Shapley, A. E., Erb, D. K., Reddy, N. A., & Pettini, M. 2005, ApJ, 626, 44
Steidel, C. C., Adelberger, K. L., Shapley, A. E., Pettini, M., Dickinson, M., & Giavalisco, M. 2000, ApJ, 532, 170
Stockton, A., Canalizo, G., & Maihara, T. 2004, ApJ, 605, 37
Stockton, A., & McGrath, E. 2007, in ASP Conf. Ser., 379, Cosmic Frontiers, ed. N. Metcalf & T. Shanks (San Francisco: ASP), 122
Stott, J. P., et al. 2010, ApJ, 718, 23
Strazzullo, V., et al. 2010, A&A, 524, A17
Sulentic, J. W., Rosado, M., Dultzin-Hacyan, D., Verdes-Montenegro, L., Trinchieri, G., Xu, C., & Pietsch, W. 2001, AJ, 122, 2993
Sun, M., Donahue, M., & Voit, G. M. 2007, ApJ, 671, 190
Suzuki, R., et al. 2008, PASJ, 60, 1347
Tadaki, K., et al. 2011, PASJ, 63, No.3872
Tamura, Y., et al. 2009, Nature, 459, 61
Tanaka, M., De Breuck, C., Venemans, B., & Kurk, J. 2010, A&A, 518, A18
Tanaka, M., Kodama, T., Arimoto, N., Okamura, S., Umetsu, K., Shimasaku, K., Tanaka, I., & Yamada, T. 2005, MNRAS, 362, 268
Thomas, D., Maraston, C., Bender, R., & Mendes de Oliveira, C. 2005, ApJ, 621, 673
Thomas, D., Maraston, C., Schawinski, K., Sarzi, M., & Silk, J. 2010, MNRAS, 404, 1775
Tokunaga, A. T., & Vacca, W. D. 2005, PASP, 117, 421
Tran, K.-V. H., et al. 2010, ApJ, 719, L126
Tran, K.-V. H., Franx, M., Illingworth, G. D., van Dokkum, P., Kelson, D. D., Blakeslee, J. P., & Postman, M. 2007, ApJ, 661, 750
Uchimoto, Y. K., et al. 2008, PASJ, 60, 683
Urquhart, S. A., Willis, J. P., Hoekstra, H., & Pierre, M. 2010, MNRAS, 406, 368
Valdés, J. R., Berta, S., Bressan, A., Franceschini, A., Rigopoulou, D., & Rodighiero, G. 2005, A&A, 434, 149
van der Werf, P. P., Moorwood, A. F. M., & Bremer, M. N. 2000, A&A, 362, 509
van Dokkum, P. G., & Franx, M. 2001, ApJ, 553, 90
van Dokkum, P. G., Franx, M., Fabricant, D., Illingworth, G. D., & Kelson, D. D. 2000, ApJ, 541, 95
Venemans, B. P., et al. 2002, ApJ, 569, L11
Venemans, B. P., et al. 2005, A&A, 431, 793
Venemans, B. P., et al. 2007, A&A, 461, 823
Wallace, L., & Hinkle, K. 1997, ApJS, 111, 445
Yagi, M., Komiyama, Y., Yoshida, M., Furusawa, H., Kashikawa, N., Koyama, Y., & Okamura, S. 2007, ApJ, 660, 1209
Yamada, T., et al. 2001, PASJ, 53, 1119
Yoshida, M., et al. 2002, ApJ, 567, 118
Yoshikawa, T., et al. 2010, ApJ, 718, 112
Zirm, A. W., et al. 2008, ApJ, 680, 224